J. Fluid Mech. (1989), *vol.* 199, *pp.* 55–88
Printed in Great Britain

Numerical simulation of the absolutely and convectively unstable wake

By K. HANNEMANN AND H. OERTEL JR
Institute for Theoretical Fluid Mechanics, DFVLR-AVA Göttingen, FRG

(Received 22 September 1987 and in revised form 4 May 1988)

The development of the wake behind a flat plate at a supercritical Reynolds number ($Re = 200$, based on the plate thickness and free-stream velocity) is simulated numerically by solving the two-dimensional unsteady Navier–Stokes equations with a finite-difference Galerkin method. The intermediate quasi-steady state of the wake development is investigated with an Orr–Sommerfeld analysis for complex frequencies and wavenumbers. Based on this linear, local stability analysis it can be shown that the quasi-steady state can be divided into regions of local absolute and local convective instability. One goal of this work is to determine the validity of the linear, local stability theory by comparing the predictions of the Orr–Sommerfeld analysis to the results of a numerical wake simulation. Based on this comparison, for the investigated flow field, the frequency selection mechanisms recently proposed by several authors are discussed. Base bleed is applied in the numerical simulation of the wake as a control parameter, following the well-known experimental result that sufficient base bleed reduces the strength of the vortex street (see e.g. Wood 1964). It can be shown that, from a critical base-bleed ratio, disturbances grow no longer in time but only in space, indicating a change of the global stability characteristics. In addition the linear, local stability analysis is used to investigate to what extent this global transition can be described.

1. Introduction

The local concept of absolutely and convectively unstable wave propagation was first introduced in the study of plasma instabilities by Twiss (1951, 1952) and Sturrock (1958) and subsequently by Briggs (1964) and Bers (1975). In recent years this concept has also been applied to hydrodynamic stability investigations. A flow is absolutely unstable if disturbance waves, generated by a pulsewise perturbation (Dirac delta function in space and time), contain amplified upstream- and downstream-travelling waves as well as one that remains at the location of its generation, while amplifying in time. One consequence of absolute instability is that the entire flow field is influenced by the impulse response for a large time. On the other hand, if the flow is convectively unstable amplified disturbance waves are convected away from the location of generation; after a sufficiently large time the basic flow is again undisturbed locally.

Koch (1983, 1985) investigated a family of wake profiles modelled with analytic functions using the local concept of absolute and convective instability. He revealed that the wake can be divided into regions of absolute and convective instability. The transition between these regions was found to occur slightly downstream of the reverse-flow region as indicated in figure 1. In the corresponding regions of absolute and convective instability, the impulse response of a one-dimensional flow is

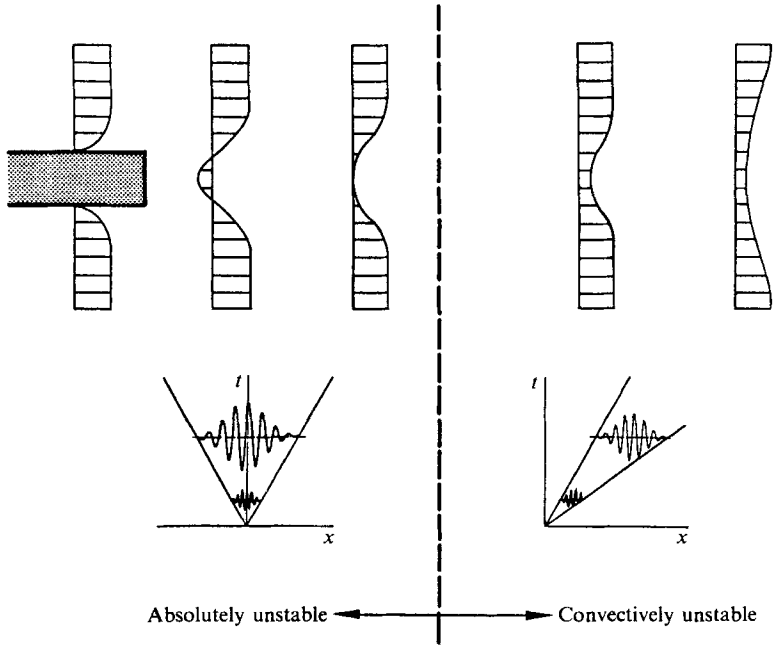

FIGURE 1. Sketch of the local wake-stability properties.

illustrated in the form of ray diagrams in the (x,t)-plane (see also §5.1). Koch (1983, 1985) suggested that the shedding frequency of the wake is governed by a direct local resonance, occurring at the location where the transition from absolute to convective instability takes place and caused by the coalescence of an upstream-travelling and a downstream-travelling mode.

Gaster (1968) investigated the physical meaning of the singularities occurring in the relation between complex frequencies and wavenumbers (dispersion relation), found by Betchov & Criminale (1966) for wake and jet profiles. He concluded that flows can exist that allow a disturbance wave to remain at the location of its generation while being amplified in time. He called the stability characteristics of such a flow a true time-growing instability; he further concluded that for such a flow no steady laminar state exists.

The local concept of absolute and convective instability has also been applied to the investigation of other shear flows. Huerre & Monkewitz (1985) showed that mixing layers become absolutely unstable if the two layers propagate in opposite directions with a velocity ratio $|u_2/u_1| > 0.136$. It was shown by Monkewitz & Sohn (1986) that hot jets are absolutely unstable. A survey and discussion of possible absolutely unstable flows is also given by Bechert (1985) and Huerre (1985). An experimental investigation concerning the absolute and convective instability of shear flows was carried out by Strykowski (1986).

Interpreting the results of Mattingly & Criminale (1972) also suggests that the near wake in their investigation was absolutely unstable. Nguyen (1986) and Monkewitz & Nguyen (1987) have applied the local concept of absolute and convective instability to a family of wake profiles modelled with analytic functions. They found that if the displacement thickness of the boundary layer separating from the body is very small, the wake can be first convectively unstable then absolutely unstable and further downstream again convectively unstable. This kind of flow is called by

Monkewitz & Sohn (1986) type 'AF', meaning absolutely unstable with a free boundary. It has two transition points between absolute and convective instability. Flows having only one transition point, where the absolutely unstable region extends to the solid boundary of the body, are called type 'AB', meaning absolutely unstable with a solid boundary. A third type of unstable flow is the completely convectively unstable flow, called type 'C'. The absolutely unstable nature of wake flows was also investigated by Triantafyllou, Triantafyllou & Chryssostomidis (1986).

An interesting question discussed by Monkewitz & Nguyen (1987) is whether there exists a connection between the above-described occurrence of absolute and convective instability in the near wake and the selection of the pure vortex-shedding frequency observed in the wake saturation state. In addition to Koch's criterion the maximum-growth criterion of Pierrehumbert (1984) and the initial-resonance criterion of Monkewitz & Nguyen (1987) have been proposed. Pierrehumbert states that the flow is dominated by the mode in the absolutely unstable region that stays at the location of its generation and has the maximum temporal growth rate. The initial-resonance criterion suggests that the shedding frequency is determined by the most upstream absolutely unstable location in the wake. A detailed discussion of the specific applications of these selection criteria in relation to the above-described local wake stability characteristics is given by Monkewitz & Nguyen (1987).

To determine whether one of the above selection criteria can be successfully applied to predict the complex frequency (i.e. the frequency and the associated temporal growth rate) in 'real wakes', linear, local stability analysis is applied to the basic state of the wake (a more complete discussion of this basic state will be given shortly). Since the basic state cannot be easily obtained experimentally at supercritical Reynolds numbers, we decided to carry out the required analysis numerically. This enables the computation of the appropriate basic state for the stability analysis. Further, the numerical wake simulation was designed to document the amplification process leading to the saturation state as well as the saturation state itself. Therefore we developed a numerical scheme, the finite-difference Galerkin method, with which we solve the unsteady, two-dimensional and incompressible Navier–Stokes equations. This scheme is based on the finite-difference Galerkin method developed for the solution of the steady Navier–Stokes equations by Stephens *et al.* (1984).

This paper is organized in the following fashion. In §2 we present the basic equations, namely the two-dimensional time-dependent incompressible Navier–Stokes equations and the Orr–Sommerfeld equation, which are used for the numerical simulation of the wake flow and the local, linear stability analysis, respectively. The numerical schemes used for the solution of these equations are described in §3. In §4 we present the results of the numerical simulation, where the development of the wake behind a flat plate at zero incidence at a supercritical Reynolds number ($Re = 200$) is discussed. In §5 a description of the local concept of absolute and convective instability is given and is then applied to the quasi-steady solution of the Navier–Stokes equations. From the quasi-steady solution the temporal amplification process begins (see §4). It therefore represents a proper basic state for the stability analysis. The location marking the transition between regions of local absolute and convective instability is presented. Further, we compare the predictions of the local, linear stability analysis with the results of the numerical simulation. This enables us to discuss whether one of the frequency selection criteria can be successfully applied to the investigated flow field. Wake control is discussed in §6, where we have numerically simulated the control of the wake using base bleed

at several base-bleed coefficients; sufficient base bleed has been shown experimentally to lead to a reduction in base drag, see e.g. Wood (1964, 1967), Bearman (1967) and Michel & Kost (1982). The stability of the wake with base bleed is also investigated using linear, local stability analysis and is discussed in terms of absolute and convective instability. Finally, in §7 we discuss our results and comment on some of the unresolved problems.

2. Basic equations

We consider a two-dimensional wake flow behind a flat plate at zero incidence with velocity vector $\boldsymbol{v} = (u, w)$ and pressure $p(x, z)$. All flow quantities are non-dimensionalized by the free-stream velocity u_∞^*, the plate thickness D^* and the fluid density ρ^*. For the incompressible flow of a Newtonian fluid confined within the region Ω, the conservation of mass and momentum can be expressed in differential form:

$$\nabla \cdot \boldsymbol{v} = 0 \quad \text{in} \quad \Omega, \tag{1}$$

$$\frac{\partial \boldsymbol{v}}{\partial t} + (\boldsymbol{v} \cdot \nabla)\, \boldsymbol{v} = -\nabla p + \frac{1}{Re} \nabla^2 \boldsymbol{v} \quad \text{in} \quad \Omega; \tag{2}$$

with Reynolds number $Re = u_\infty^* D^*/\nu^*$, where ν^* is the kinematic viscosity. On the boundary Ω_R of the integration domain Ω, the velocity $\boldsymbol{v}$ is equal to the boundary-value vector $\boldsymbol{v}_R$:

$$\boldsymbol{v} = \boldsymbol{v}_R \quad \text{on} \quad \Omega_R. \tag{3}$$

The specified boundary data $\boldsymbol{v}_R$ must satisfy

$$\int_\Omega \nabla \cdot \boldsymbol{v} \, \mathrm{d}\Omega = \int_{\Omega_R} \boldsymbol{v}_R \cdot \boldsymbol{n} \, \mathrm{d}\Omega_R = 0, \tag{4}$$

where $\boldsymbol{n}$ is the normal vector on the boundary Ω_R.

To investigate the stability characteristics of the computed flow fields we apply the classical linear, local stability analysis for viscous flows. Following this approach, the disturbances superposed on the basic state are described by a complex perturbation stream function of the form

$$\tilde{\psi}(x, z, t) = \hat{\psi}(z)\, \mathrm{e}^{\mathrm{i}(\alpha x - \omega t)}, \tag{5}$$

where α and ω are the complex wavenumbers and frequency respectively; $\hat{\psi}(z)$ is the complex amplitude function. The derivation discussed in detail by e.g. Schlichting (1982) and Drazin & Reid (1981) leads finally to the Orr–Sommerfeld equation

$$(u_0 - c)\left(\frac{\partial^2 \hat{\psi}}{\partial z^2} - \alpha^2 \hat{\psi}\right) - \frac{\partial^2 u_0}{\partial z^2} \hat{\psi} + \frac{\mathrm{i}}{\alpha\, Re}\left(\frac{\partial^4 \hat{\psi}}{\partial z^4} - 2\alpha^2 \frac{\partial^2 \hat{\psi}}{\partial z^2} + \alpha^4 \hat{\psi}\right) = 0, \tag{6}$$

which together with boundary conditions chosen appropriately for the investigation of wake profiles,

$$\hat{\psi} = \hat{\psi}' = 0 \quad \text{at} \quad z = \pm\infty, \tag{7}$$

defines the stability eigenvalue problem; the phase velocity $c = \omega/\alpha$.

3. Numerical methods

3.1. *Finite-difference Galerkin method*

The time-dependent, incompressible Navier–Stokes equations (1) and (2) together with the boundary conditions (3), are integrated numerically in primitive variables with a finite-difference Galerkin method, introduced by Stephens *et al.* (1984) for the solution of the steady Navier–Stokes equations. We selected this method for the simulation of the wake because it allows the elimination of the pressure, thereby requiring only the specification of the velocity on the boundaries. Therefore a straightforward application of the no-slip condition can be applied on the plate; we believe this to be important because of the absolutely unstable nature of the flow in this region. As poined out by Davis & Moore (1982) and Gentzsch & Schwamborn (1985) numerical diffusion (i.e. additional terms with the form of the physical diffusion term, introduced inherently or explicitly owing to the spatial discretization or to stability considerations, change the physical diffusion) must be avoided in separated flows. Hence we have employed central differencing.

The finite-difference Galerkin method enables the removal of the discrete pressure by projecting the discretized Navier–Stokes equations into a divergence-free subspace using a Galerkin technique. Consider the following discretized form of the Navier–Stokes equations and the boundary conditions at time step t_n:

$$\nabla_h \cdot \boldsymbol{v}^h = 0 \qquad \text{on} \quad \omega_h, \tag{8}$$

$$\frac{\partial \boldsymbol{v}^h}{\partial t} + (\boldsymbol{v}^h \cdot \nabla_h)\, \boldsymbol{v}^h = -\nabla_h p^h + \frac{1}{Re} \nabla_h^2 \boldsymbol{v}^h \quad \text{on} \quad \Omega_h, \tag{9}$$

$$\boldsymbol{v}^h = \boldsymbol{\beta}^h \qquad \text{on} \quad \Omega_{R_h}; \tag{10}$$

with the index h indicating discrete quantities, spaces and operators. The boundary data are given by $\boldsymbol{\beta}^h$.

The equations are discretized on a staggered grid; Ω_h and ω_h represent the inner mesh points for vectors and scalar quantities respectively and Ω_{R_h} contains the mesh points on the boundary (see figure 2). The discrete gradient and divergence operators must be adjoint in order to eliminate the pressure from the system of equations. In our application this was achieved by using central differencing on the staggered grid. The following discrete approximation can be made for the velocity vector:

$$\boldsymbol{v}^h = \boldsymbol{r}^h + \sum_{i=1}^{m} a_i(t)\, \boldsymbol{\Phi}_i^h, \tag{11}$$

where $\boldsymbol{\Phi}_i^h$ are the discrete divergence-free base functions defined on Ω_h only. For a uniform grid containing n^2 inner grid points the base functions are defined as follows (see Stephens *et al.* 1984):

$$\begin{aligned}
\boldsymbol{\Phi}_{i,j}^{l+\frac{1}{2},\, m+\frac{1}{2}} &= (1,-1)^t, && i = l, j = m,\\
&= (1,1)^t, && i = l+1, j = m,\\
&= (-1,1)^t, && i = l+1, j = m+1,\\
&= (-1,-1)^t, && i = l, j = m+1,\\
&= (0,0)^t, && \text{all other } i,j,\\
& l = 1,\ldots,n-1; \quad m = 1,\ldots,n-1.
\end{aligned} \tag{12}$$

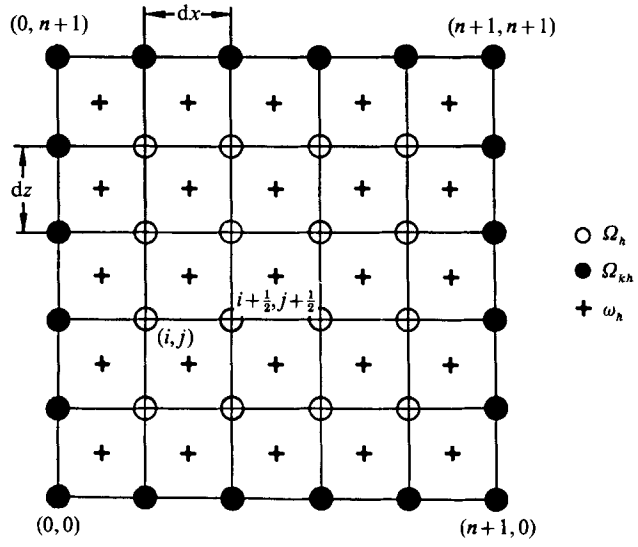

FIGURE 2. Definition of the discrete spaces.

On the boundary Ω_{R_h}, these internal base functions are zero. The boundary vector $\boldsymbol{r}^h$ must fulfil the boundary conditions (10) and can be expressed with a sum similar to that in (11). The structure of the base functions remains unchanged, except that they must be defined on the boundary. The boundary vector can easily be computed for Dirichlet boundary conditions; however, if the boundaries are time-dependent, $\boldsymbol{r}^h$ must be recalculated after each time step. The system of equations for determining the unknown coefficients a_i can be derived with a discrete Galerkin technique, i.e. the scalar product of (9) with every base function must be zero:

$$\left(\frac{\partial \boldsymbol{v}^h}{\partial t}+(\boldsymbol{v}^h\cdot\nabla_h)\,\boldsymbol{v}^h+\nabla_h p^h-\frac{1}{Re}\nabla_h^2\,\boldsymbol{v}^h,\boldsymbol{\Phi}_i^h\right)_{\Omega_h}=0,\quad i=1,\ldots,m. \tag{13}$$

Using a discrete analogue of integration by parts the component of the scalar product containing the pressure can be written as

$$(\nabla_h p^h,\boldsymbol{\Phi}_i^h)_{\Omega_h}=(p^h,\boldsymbol{\Phi}_i^h)_{\Omega_{R_h}}-(p^h,\nabla_h\cdot\boldsymbol{\Phi}_i^h)_{\omega_h}=0,\quad i=1,\ldots,m. \tag{14}$$

The base functions are divergence free and vanish on Ω_{R_h}. Therefore the pressure is eliminated from the system of equations and we solve only

$$\left(\frac{\partial \boldsymbol{v}^h}{\partial t}+(\boldsymbol{v}^h\cdot\nabla_h)\,\boldsymbol{v}^h-\frac{1}{Re}\nabla_h^2\,\boldsymbol{v}^h,\boldsymbol{\Phi}_i^h\right)_{\Omega_h}=0,\quad i=1,\ldots,m. \tag{15}$$

The integration in time is performed with explicit Runge–Kutta time stepping. Therefore all quantities at the time step t_n are known and the system

$$Ma_t=f \tag{16}$$

must be solved for the time derivative a_t of the coefficient a. The right-hand side f contains the contribution of the convective and the diffusion term. It can be shown that the matrix M is symmetric and positive definite. The solution of a_t is found iteratively by a conjugate gradient method (see Schwarz, Rutishauser & Stiefel 1968 and Khosla & Rubin 1981).

We restricted ourselves here to a description of the finite-difference Galerkin method using a uniform mesh only. Arbitrary geometries with non-uniform mesh can be handled by transforming them onto a computational space with uniform mesh, where the algorithm just described can then be applied. For more details concerning this transformation the reader is referred to Stephens *et al.* (1984).

3.2. *Chebyshev collocation method*

In order to solve the temporally and spatially amplified Orr–Sommerfeld eigenvalue problem (6), (7), we adopt the Chebyshev collocation method (Chebyshev Matrix Method) introduced by Gottlieb, Hussaini & Orszag 1984). Laurien (1986) and Koch (1986) employed this method to investigate the Blasius boundary layer and Poiseuille flow. Here we introduced further modifications to accommodate wake-type profiles. The unknown amplitude function $\hat{\psi}(z)$ should be obtained in the range $[-\infty,\infty]$. The numerical simulation of the wake is, however, carried out in an integration domain with finite extent in the z-direction. Therefore the range in which the amplitude function is computed is chosen to be $[-H,H]$, where H is the distance of the upper and lower boundary of the integration domain from the centreline. We use Chebyshev polynomials $T_K(\eta)$ of order K to approximate $\hat{\psi}(z)$ in the transformed coordinate $\eta = \eta(z)$:

$$\hat{\psi}(\eta) = \sum_{K=0}^{N-1} b_K T_K(\eta). \tag{17}$$

The range $[-H,H]$ is therefore mapped into $[-1,1]$ via an exponential transformation. The approximation of $\hat{\psi}(z)$ and its derivatives is not performed using an expansion with respect to the Chebyshev coefficients b_K. Instead we apply the Chebyshev collocation method to obtain directly the values of $\hat{\psi}(z)$ at the collocation points:

$$\eta_j = \cos\frac{\pi j}{N-1}; \quad j = 0,\ldots,N-1. \tag{18}$$

To distinguish between absolute and convective instability, we need the eigenvalue spectrum of the Orr–Sommerfeld equation for complex wavenumber α and complex frequency ω.

4. Numerical wake simulation

The dashed line in figure 3 defines the integration domain for the unsteady wake simulation using the finite-difference Galerkin method. In all the computations presented the flow is from left to right.

The left boundary is chosen to be $5D$ ($D = 1$ is the plate thickness) upstream and the right boundary $13D$ downstream of the trailing edge of the plate. The upper and lower boundaries are located at a distance of $18D$ from the centreline. To obtain sufficiently good boundary conditions for the left, upper and lower boundaries, the flow is first computed around the whole plate in the upper half-plane (see figure 3). For this purpose symmetry conditions on the centreline are used. At the left and upper boundary of this integration domain, $20D$ upstream from the leading edge and $50D$ above the centreline respectively, free-stream conditions $u = 1, w = 0$ are applied. The half-domain computation is carried out by solving the unsteady Navier–Stokes equations. However, owing to the symmetry conditions applied on the centreline computation of vortex shedding is not possible. Nevertheless it is important to compute the solution around the whole plate in the upper half-plane to

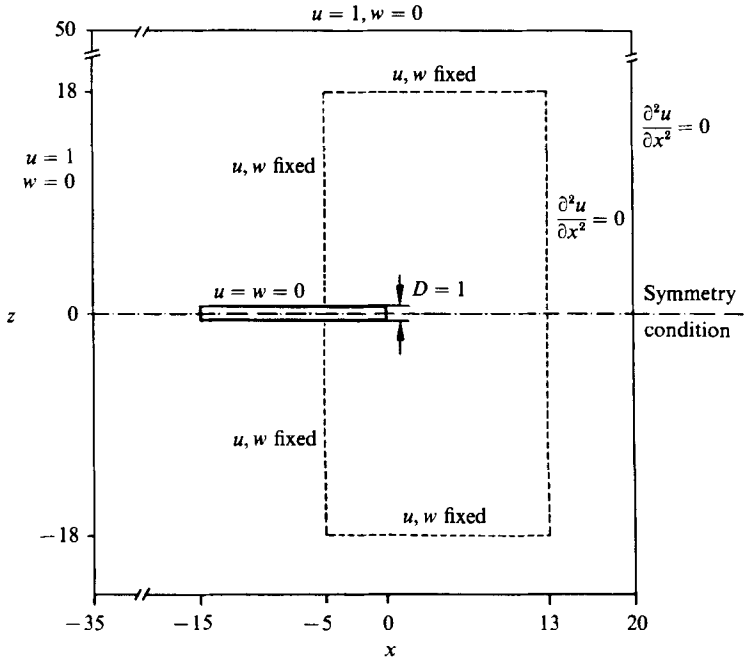

FIGURE 3. Integration domains and boundary conditions.

obtain boundary conditions for the left, upper and lower boundary of the full integration domain (dashed line) that properly describe the displacement of the flow due to the presence of the plate and the development of the boundary layer on the plate. It seems worth mentioning that the potential solution was applied as a fixed boundary condition on the upper and lower boundaries of the integration domain, framed by the dashed line, at $z = \pm 18$; however, the results proved to be unsatisfactory. The velocity field did not asymptotically approach the potential-flow conditions applied on the boundary.

The left, upper and lower boundaries of the full domain (dashed line) are chosen to be sufficiently far away from the trailing edge and the centreline, respectively, that the fluctuations caused by vortex shedding can be neglected. Typically, in the saturation state, the r.m.s. fluctuations at these outer boundaries are more than two orders of magnitude lower than the maximum r.m.s. fluctuations occurring in the wake. For this reason fixed (time-independent) boundary conditions are applied. At the downstream boundaries the u-velocities are extrapolated after every time step with the condition

$$\frac{\partial^2 u}{\partial x^2} = 0. \tag{19}$$

Numerical tests have shown that (19) is most suitable because it produces minimum upstream influence in the simulation of the wake. After computing the w-velocities using (11) it is determined whether the extrapolated velocities satisfy condition (4); this was found to be the case for all the simulations.

After the boundary conditions for the integration domain, defined by the dashed line in figure 3, could be determined an initial flow field was first computed with fixed velocity values on the whole boundary, leading to a flow field similar to the one in figure 8 at $t = 0$. Before the wake simulation with a flexible outflow boundary

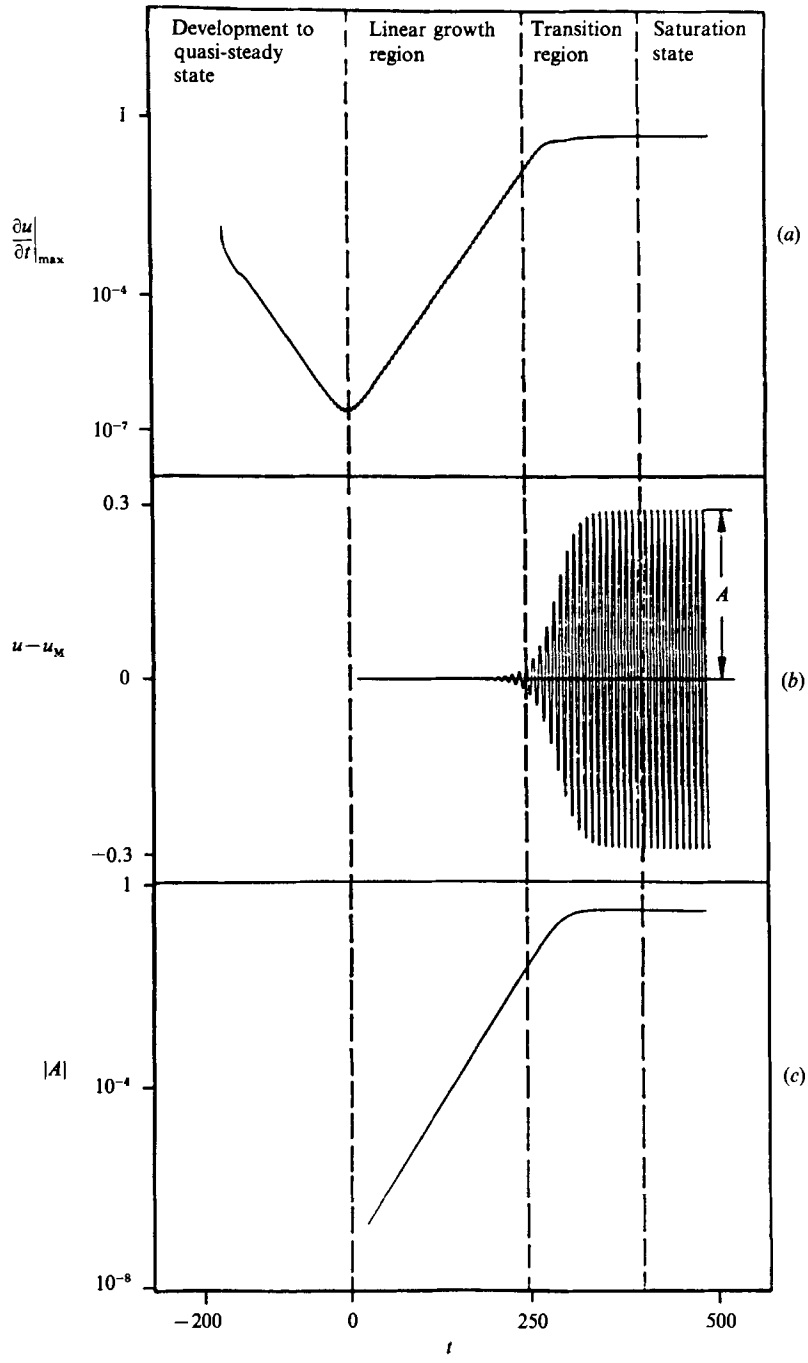

FIGURE 4. Temporal development of the wake, $Re = 200$. (*a*) Maximum time derivative $\partial u/\partial t$ in the flow field; (*b*) u-Velocity component at $x = 3.9, z = 0.625$; (*c*) Absolute value of the amplitude.

condition is started the initial flow field is made symmetric about the centreline to reduce the perturbation level as much as possible.

Figure 4 shows the temporal development of the numerical simulation at $Re = 200$. Figure 4(*a*) shows the maximum time derivative of the u-velocity component in the integration domain as a function of the non-dimensionalized time

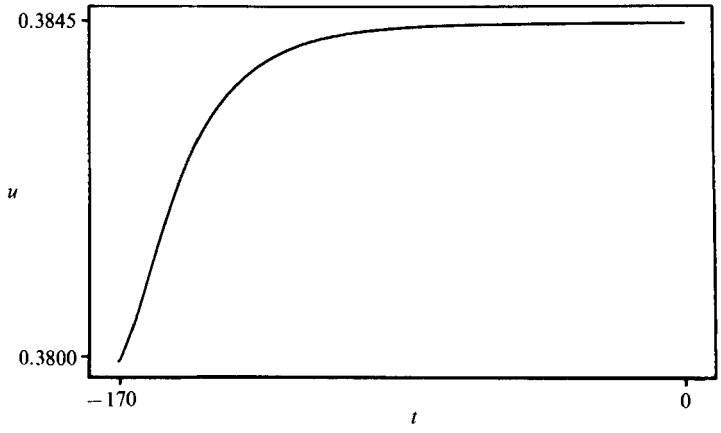

FIGURE 5. u-Velocity component at $x = 3.9, z = 0.625$ during the development to the quasi-steady state.

$t = t^* u_\infty^* / D^*$. This diagram can only explain how 'steady' the entire flow is and cannot be directly related to the development of the flow at one point. Therefore the oscillations occurring during the growth of $(\partial u/\partial t)_{\max}$ (figure 4*a*) have no physical meaning. However, they are caused by the oscillations in the wake and have the same frequency. In figure 4 one can distinguish four domains: the development to a quasi-steady state; the linear growth region; a transition region to the saturation state; and the nonlinear saturation state.

After starting the simulation ($t = -171$) the development toward the steady solution of the Navier–Stokes equations is seen. The steady solution, however, cannot be reached because the time-dependent simulation is carried out at a supercritical Reynolds number and hence the flow is unstable and even infinitesimal perturbations are amplified. However, we define a quasi-steady state to exist at $t = t_0 = 0$ in figure 4(*a*). A characteristic development of the velocity at one location in this first domain can be seen in figure 5, where the u-velocity component at the point $x = 3.9, z = 0.625$ is plotted. It can be seen that the velocity value converges quickly to that of the quasi-steady state.

Experimentally, the amplification of the perturbations begins at an amplitude commensurate with the background turbulence level. Numerically, an equivalent 'numerical fluctuation level' exists which depends on the choice of the initial condition, the spatial discretization, and, in the case of the finite-difference Galerkin method, is also a function of how accurately the system of equations (16) is solved iteratively. Although both represent a source of perturbations, it is clear that the 'numerical fluctuation level' is by no means a direct simulation of the turbulence level present in a wind tunnel. This can, for example, be seen by investigating the spatial distribution of the background fluctuations. In a wind-tunnel test section their distribution can be regarded as approximately uniform, whereas in the numerical simulation the fluctuation level depends on the computational grid which, in our wake simulation, is not uniform in the z-direction. The highest error due to the spatial discretization occurs in the regions, about $6D$ above and below the centreline, where the change of the grid size is largest.

In the simulation in figure 4 we started with a symmetric flow field and (16) was solved to an accuracy of $\epsilon = 10^{-9}$; correspondingly the growth of the time derivative commences after it has reached a value of about 10^{-7}. Using a higher ϵ, or an initial

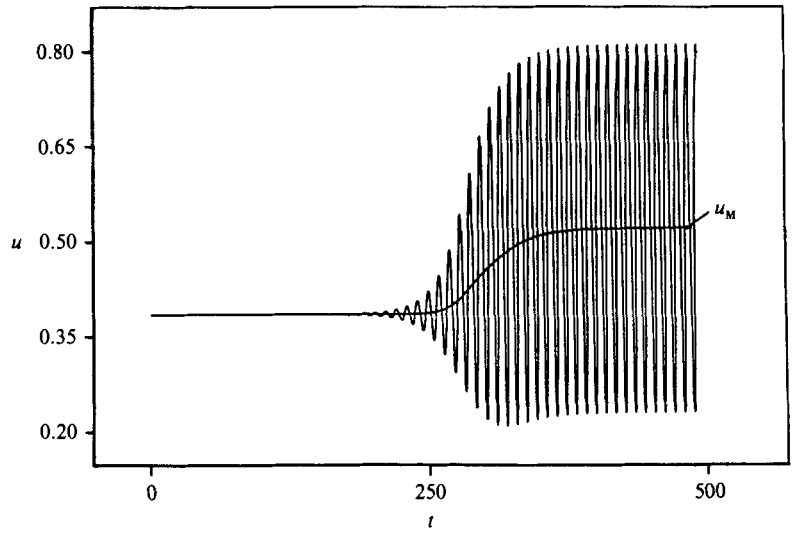

FIGURE 6. Development of the u-velocity component at $x = 3.9, z = 0.625$ and $u_M(t)$.

flow field that was not forced to be symmetric about the centreline, resulted in a higher initial 'numerical fluctuation level'. The starting process of the wake development is still dictated by the two contrary tendencies to reach the steady solution of the Navier–Stokes equations as well as the growth of disturbances in time. The exponential amplification rate as well as the initially selected frequency of the perturbations are also not affected by these changes. However, the amount of time needed to detect the amplification process in the simulation is now decreased owing to the higher initial 'numerical fluctuation level'. Clearly, to facilitate the vortex-shedding state artificial high disturbances can be introduced thereby passing the quasi-steady state in figure 4(*a*). Such time-saving techniques have been employed by many authors, e.g. by Braza, Chassaing & Ha Minh (1986) and Sun, Shen & Zhu (1988). As we shall subsequently show, the investigated wake flow can be regarded as a self-excited oscillator and hence even when the 'numerical fluctuation level' is reduced the saturation state cannot be avoided, but the time required to reach this state will then be increased.

The temporal development of the u-velocity component, at one point in the flow field, is shown in figure 4(*b*, *c*). The velocity signal in figure 4(*b*) is obtained by subtracting the mean velocity u_M from the instantaneous u-velocity value (see figure 6). From figure 4(*b*, *c*) it is clear that a well-defined exponential growth rate of the fluctuations occurs simultaneously with the increase of the maximum $\partial u/\partial t$. We define the linear growth region to exist where there is a well-defined exponential growth in time.

The constant exponential growth rate occurring at one onset frequency is the same everywhere in the wake. This can be seen from figure 7 where, as a characteristic result, the absolute value of the amplitude at $z = 2.0$ is shown as a function of the time and the coordinate x. The simulation reveals that even at the grid points that are located next to the trailing edge of the plate the same slope of $|A|$ versus t is obtained.

An interesting exception is revealed by the u-velocity fluctuations on the centreline of the wake. This will be discussed later in this section in connection with the presentation of the perturbation flows. In the transition region to the saturation

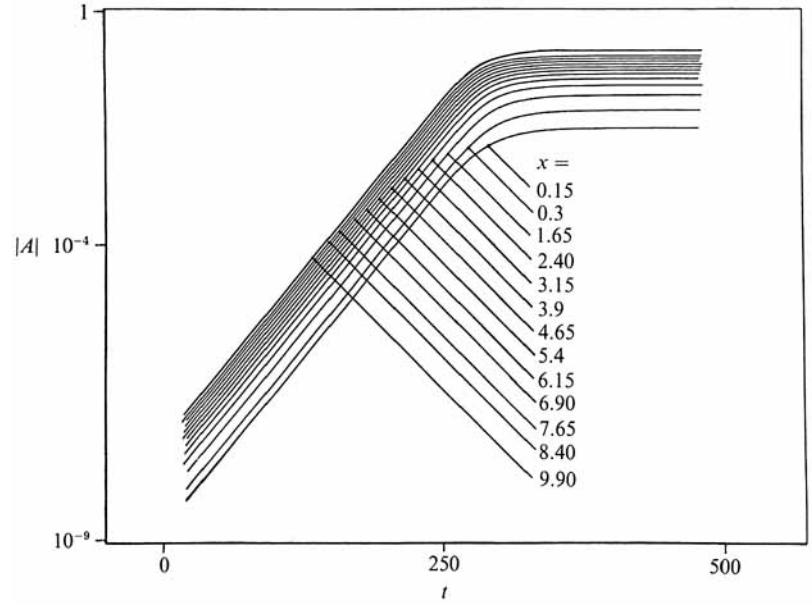

FIGURE 7. Absolute value of the amplitude as a function of the time and the coordinate x at $z = 2.0$.

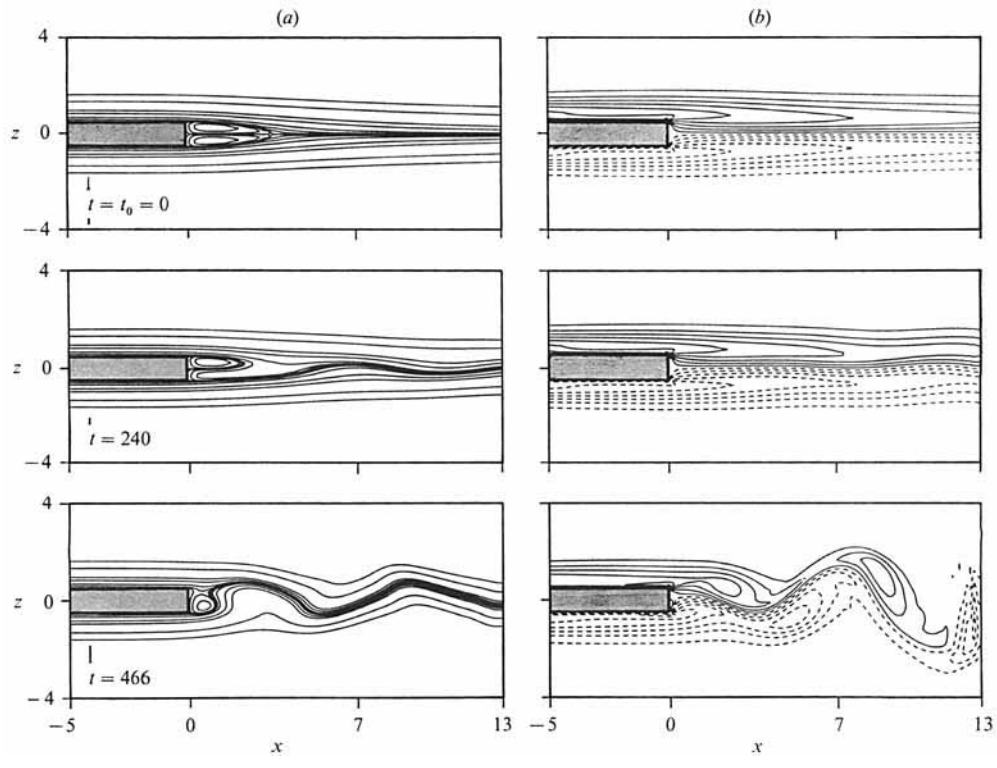

FIGURE 8. Temporal development of the wake in terms of (*a*) instantaneous streamlines and (*b*) lines of constant vorticity.

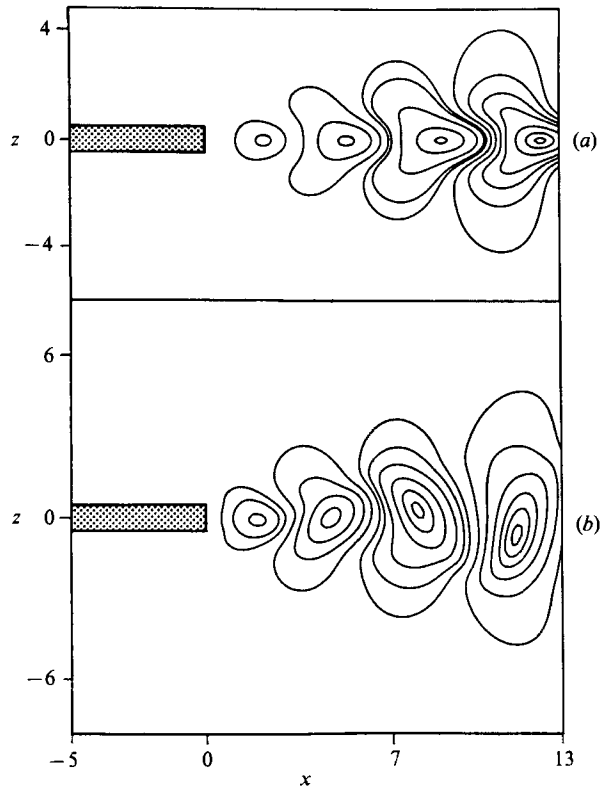

FIGURE 9. Instantaneous perturbation streamlines in (*a*) the linear growth region and (*b*) the saturation state.

state the linear growth rate is arrested by nonlinear effects which become significant; in figure 4(*c*) the nonlinearities begin to alter the linear growth rate when the amplitude $A \approx 0.01u_\infty$. These nonlinear effects lead to the saturation state commonly referred to as the Kármán vortex street. Figure 8 shows the development of the wake flow in terms of instantaneous streamline plots and the corresponding lines of constant vorticity; negative vorticity is marked by solid lines, positive vorticity by dashed lines. At time t_0 the streamline pattern of the quasi-steady solution shows a symmetric reverse-flow region extending $3.6D$ downstream of the trailing edge. The first effect, seen in the streamline plots occurring for $t > t_0$, is a change in the topological structure of the streamline patterns at the saddle point located at the end of the reverse-flow region. Here the symmetry is removed and the reverse-flow region breaks open. This has been called the saddle-point instability by Sun *et al.* (1988). The time sequence in figure 8 also shows the flow at the end of the linear growth region at $t = 240$ and the Kármán vortex street at $t = 466$.

The structural changes which occur during the transition from the linear growth region to the saturation state can best be observed by analysing the perturbation flow (see also Hannemann & Oertel 1986, 1987). For this purpose the instantaneous perturbation streamlines are plotted in figure 9; the perturbation flows are obtained by subtracting the mean flow from the instantaneous flow. In figures 10 and 11 streamline plots and u-velocity profiles of the quasi-steady flow field and the mean flow in the saturation state are shown. From these plots we conclude that the mean flow changes continuously during the development to the saturation state. For this

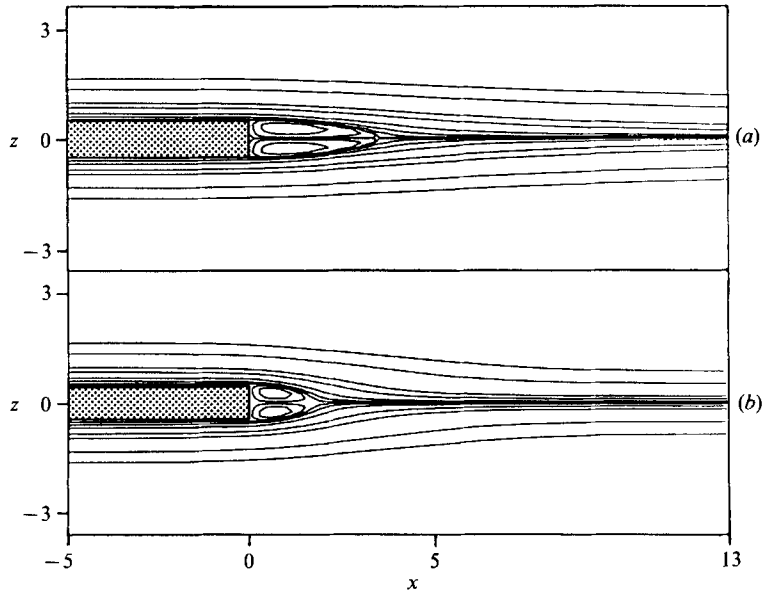

FIGURE 10. Streamlines of (*a*) the quasi-steady flow and (*b*) the mean flow in the saturation state.

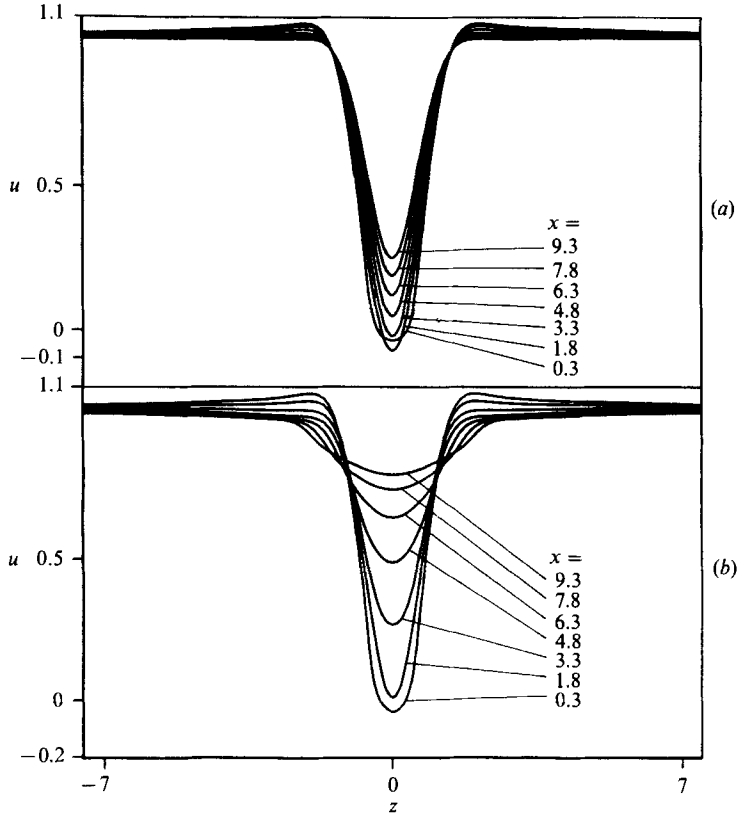

FIGURE 11. *u*-Velocity profiles of (*a*) the quasi-steady flow and (*b*) the mean flow in the saturation state.

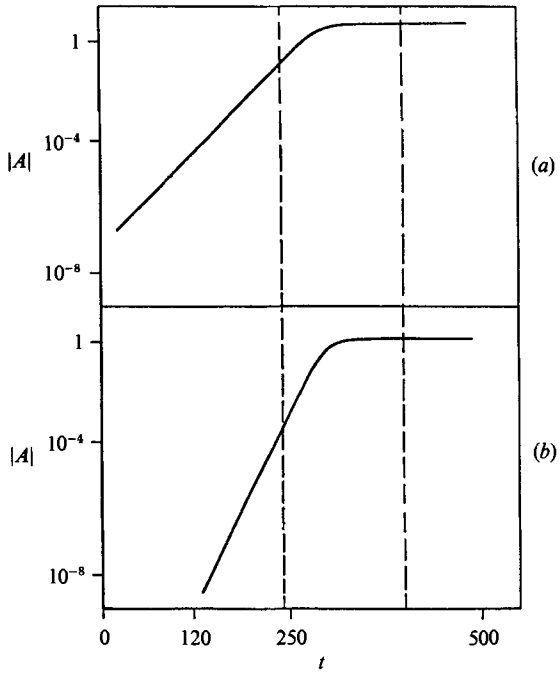

FIGURE 12. Development of the amplitude of the u-velocity component at (a) $x = 3.9, z = 0.625$ and (b) on the centreline at $x = 3.9$.

reason the appropriate mean flow necessary for the computation of the perturbation flow can only be obtained at the beginning of the wake development in the linear growth region and in the saturation state.

In the linear growth region the vortex centres of the perturbation flow lie on the centreline of the wake and the vortices rotate alternately, clockwise and counterclockwise; see figure 9(a). In the transition region the structure changes to the well-known staggered arrangement of the Kármán vortex street which can be observed in figure 9(b); here the perturbation streamlines in the saturation state are shown.

From the perturbation streamlines in figure 9(a) it can be seen that the u-velocity fluctuations on the centreline must be zero until the staggering of the vortices begins. However, w-velocity fluctuations are present and are amplified with the same amplification rate as the u-velocity fluctuations off-centreline. The development of the amplitude of the u-velocity fluctuations on the centreline is compared in figure 12 with the development shown in figure 4(c). It becomes clear that at $x = 3.9$ no periodic fluctuation can be detected until $t = 120$. As a consequence of the staggering the Strouhal number of the centreline, based on the u-velocity signals, is at once twice the onset frequency off-centreline. It can also be seen from figure 12 that the growth rate at the wake centreline is exactly twice the growth rate found everywhere else in the flow field. Investigating the development of the vortex street behind circular cylinders next to the centreline more close, P. J. Strykowski (1987, private communication) was able to confirm this result experimentally. Similarly to figure 7, it can be observed from figure 13 that the double growth rate is constant everywhere on the centreline. It is also clear from figure 13 that the staggering does not occur immediately for all x-positions. It is detected first at $x = 11.4$ and, after a period of $\Delta t \approx 70$, is observable at the grid point next to the plate. The end of the linear growth

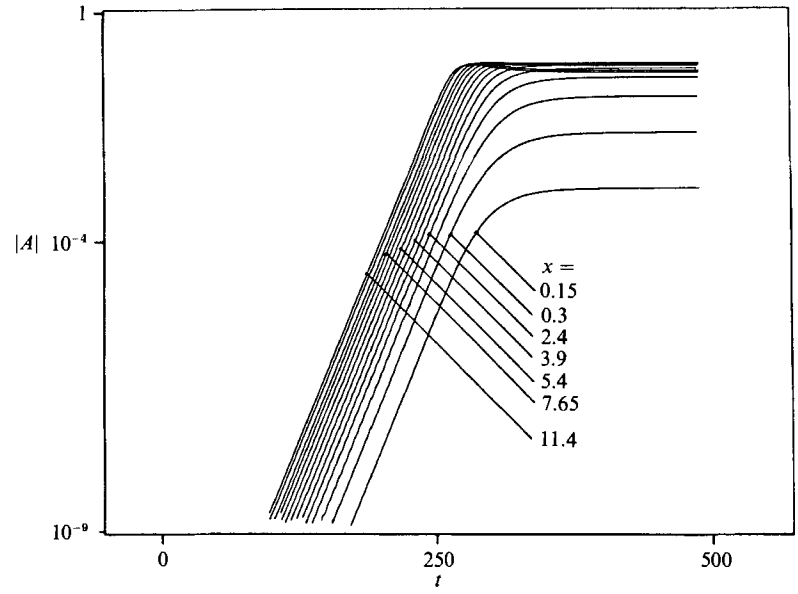

FIGURE 13. Absolute value of the amplitude as a function of the time and the coordinate x on the centreline.

region, defined by the time when the exponential growth is arrested, turns out to be the same on and off the centreline.

In the whole linear growth region the staggering is so small that the double frequency can only be detected on the grid points lying on the centreline. In the saturation state, when the staggered arrangement of the vortices is fully developed, the u-velocity signals recorded at one x-position and at several z-positions show a continuous change from one frequency far away from the centreline to the double frequency on the centreline. This fact is well known from many experimental investigations (see e.g. Kovasznay 1949).

As we shall see in §5.2 linear, local stability analysis as well as two-dimensional linear stability analysis, used by Jackson (1987) for the investigation of the transition from a steady to a periodic flow past bodies of various shapes, show that the perturbation streamlines of the wake reveal the same symmetric pattern as shown in figure 9(*a*). Therefore the commencement of the staggering is the first indication of nonlinearity. An explanation for the double growth rate on the centreline based on a stability analysis can be derived from Stuart (1960). He investigated the nonlinear mechanics of disturbances in parallel flows and suggested that the occurrence of a first harmonic of the basic perturbation due to nonlinearity is a quadratic effect. Another consequence of the nonlinearity can be observed by monitoring the oscillation frequency during the period of growth. In figure 14 it is shown that the dimensionless frequency, the Strouhal number $St = f^*D^*/u_\infty^*$, is constant during linear growth, rises rapidly when the nonlinearity becomes significant in the transition region, and finally reaches a constant value in the saturation state. The same behaviour occurs on the centreline if the Strouhal number is computed using the u-velocity signals. The onset frequency as well as the saturation frequency are then exactly twice the values off the centreline. A similar behaviour has been found experimentally for the time-dependent flow behind a circular cylinder; see Strykowski (1986) and Provansal, Mathis & Boyes (1986). It

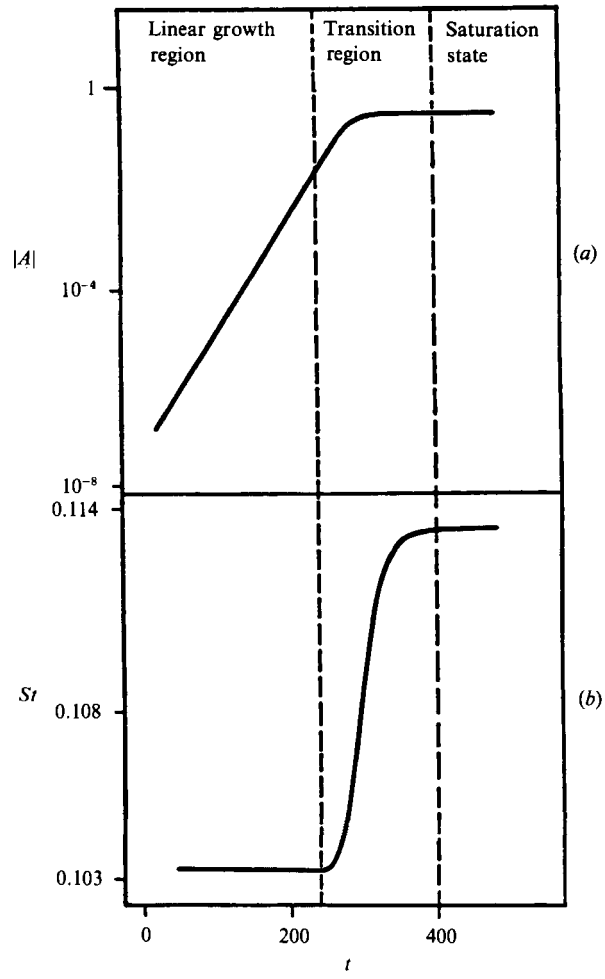

FIGURE 14. (*a*) Absolute value of the amplitude and (*b*) Strouhal number St versus time t.

should be mentioned that everywhere in the flow field the frequency increase is non-trivial and according to the numerical simulation is on the order of 10%. The data taken by Strykowski (1986) show that the difference between the onset frequency and the saturation frequency increases with Reynolds number. He found for instance that at $Re = 80$ the onset frequency already differs by 42% from the saturation frequency.

The orthogonal grid for the above-described simulation contains 122×101 points in the x- and z-directions respectively. It is uniform in the x-direction ($\Delta x = 0.15$) and highly stretched in the z-direction ($\Delta z_{\min} = 0.125$) in order to provide the best possible numerical resolution in the boundary layer and wake region. It was verified, as pointed out in detail by Hannemann (1988), that a better resolution using a grid with 166×151 points as well as the use of a longer integration domain has negligible influence on the results.

A constant time step of $\mathrm{d}t = 0.03$ is used throughout the simulation. It was found that the simulation does not depend on either the temporal integration scheme (Runge–Kutta time stepping of 2nd and 4th order was used) or on the time step as long as it fulfils the stability requirement of the Runge–Kutta scheme.

To test the influence of the outflow boundary condition (19) on the amplification of perturbations, a fixed outflow boundary condition was used. Even under this rather restrictive outflow condition the wake instability and the amplification rate and onset frequency were the same as with the flexible outflow conditions. This suggests that the outflow boundary conditions used have a very weak influence on the temporal behaviour of the disturbances.

Using the 122×101 grid with 2nd-order Runge–Kutta time stepping ($\epsilon = 10^{-9}$, accuracy to which (16) is solved iteratively) the CPU time per time step and grid point is 3.6×10^{-4} s on a CRAY-1/S, resulting in a total run time from the quasi-steady state to the saturation state of about twenty hours.

Further, the saturation frequency obtained from the numerical simulation can be compared to the experimental data from Hannemann, Lynn & Strykowski (1986), taken at the same flow conditions as in the simulation. The computed Strouhal number $St = 0.113$ agrees well with the measured value of $St = 0.116$.

5. Stability analysis

5.1. *Absolute and convective instability*

The stability characteristics of a flow can be determined by investigating its impulse response. An impulse ideally contains modes of all frequencies and wavenumbers from which the flow amplifies the mode or band of modes that is unstable. In hydrodynamic stability investigations the impulse response was investigated by Gaster (1968), based on an Orr–Sommerfeld analysis, and by Huerre & Monkewitz (1985) who considered inviscid shear flows. From these investigations it is shown that the asymptotic large-time behaviour of the impulse response based on linear, local stability theory can be summarized as follows. On each ray $x/t = \text{const}$ in the (x, t)-plane (see figure 1) the mode with the wavenumber α^*, given by

$$\frac{\mathrm{d}\omega}{\mathrm{d}\alpha}(\alpha^*) = \frac{x}{t}, \tag{20}$$

where $\mathrm{d}\omega/\mathrm{d}\alpha$ is the complex group velocity, emerges and is amplified with the growth rate

$$\sigma_i = \omega_i(\alpha^*) - \alpha_i^* \frac{\mathrm{d}\omega}{\mathrm{d}\alpha}(\alpha^*). \tag{21}$$

To determine whether the flow is convectively or absolutely unstable we must search for points of the dispersion relation for complex wavenumbers and frequencies where $\mathrm{d}\omega/\mathrm{d}\alpha = 0$. From (20) it follows that under these circumstances the mode remains at the location of its generation and therefore, according to (21), depending on the value of ω_i, the 'local' mode is amplified or damped. Betchov & Criminale (1966) and Mattingly & Criminale (1972) showed that the dispersion relation for wake profiles contains points where the group velocity is zero. These singularities occur where an upstream- and a downstream-travelling mode coalesce. For the determination of these singularities, which are in general branch points of order two, the pinching requirement must be fulfilled (see Bers 1975). The concept of absolute and convective instability is based on the location of these branch points in the complex ω-plane. It has been applied by Briggs (1964) and Bers (1975) and can be formulated as follows: an unstable flow is absolutely unstable if the branch-point singularities of its dispersion relation lie in the upper half of the complex ω-plane ($\omega_i > 0$); if they lie in the lower half-plane ($\omega_i < 0$) the flow is convectively unstable. In figure 1 the impulse

responses for an absolutely unstable and a convectively unstable flow are sketched in the (x, t)-plane.

The generated wave packet is bounded by two rays having zero amplification ($\sigma_i = 0$). Inside the wedge disturbances grow exponentially and outside they are damped. The type of instability can also be determined equivalently by locating the position of the ray $x/t = 0$. If this ray lies inside the wedge of amplified wavenumbers the flow is absolutely unstable and the corresponding wavenumber is amplified in time at the location of its generation; disturbances also amplify upstream and downstream. For convective instability the ray $x/t = 0$ lies outside the amplified wedge and therefore local disturbances are damped.

It should be mentioned here that the terminology of absolute and convective instability can only be used within a particular reference frame (see Landau & Lifshitz 1959). Therefore we shall discuss the stability characteristics in a reference frame fixed with respect to the flat plate.

5.2. *Orr–Sommerfeld analysis*

The Orr–Sommerfeld stability analysis is based on the investigation of small-amplitude disturbances superposed on a basic state. It therefore can *a priori* only be applied for the investigation of flows near the critical Reynolds number or near the onset of the instability as long as the amplitudes of the perturbations are small. From this it follows that the basic state chosen for our analysis must be the quasi-steady solution of the Navier–Stokes equations.

It has already been mentioned in §2.2 that in the theory of the linear, local stability analysis the basic state is considered to be locally parallel. This assumption is not fulfilled in the near-wake region. In the vicinity of the trailing edge and near the saddle point at the end of the reverse-flow region the variation of the u-velocity profiles in the downstream direction cannot be neglected; further downstream however the parallel-flow assumption is approximately fulfilled. Nevertheless, given the simplifying assumptions, it is very important to compare the predictions of the linear, local stability theory using the appropriate basic state with the results of the numerical simulation.

In figure 15 the eigenvalues of the combined stability analysis are plotted in the complex α-plane for the u-velocity profile of the quasi-steady solution at $x = 4.0$; only the symmetric modes (Kármán modes) are presented.

The branch-point singularity for the investigated velocity profile (in figure 15) has a positive temporal growth rate ω_i and therefore according to the concept of absolute and convective instability the profile is absolutely unstable. To find the transition point between absolute and convective instability in the wake we computed the eigenvalue spectrums for several u-velocity profiles in the near-wake region and tracked the location of the branch-point singularities. The temporal amplification rate ω_i, and frequency ω_r occurring at the branch-point singularities are plotted in figure 16 as a function of the distance from the trailing edge.

It is clear from figure 16 that the region of absolutely unstable velocity profiles extends from the flat plate to approximately $x = 4.56$. According to the classification given by Monkewitz & Sohn (1986) the flow is of type 'AB', meaning absolutely unstable with a solid boundary. The velocity profile separating the region of absolute and convective instability has a centreline velocity $u_{CL} = 0.04$. Hence the transition to convective instability occurs slightly downstream of the reverse-flow region, as previously described by Koch (1985). Using a modified hyperbolic-tangent wake model he found the centreline velocity at the transition point to be $u_{CL} = 0.03$.

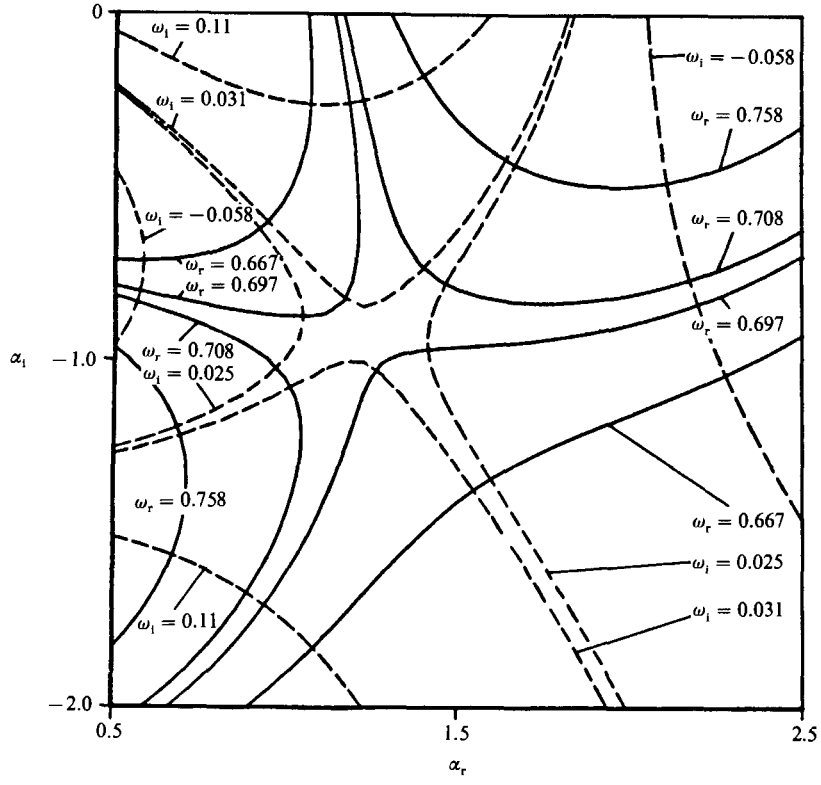

FIGURE 15. Eigenvalues of the symmetric mode; u-velocity profile at $x = 4.0$.

Monkewitz & Nguyen (1987) found that absolute instability is possible up to a centreline velocity of $u_{CL} = 0.09$.

The change of the wake profiles in the downstream direction can be well described by considering the development of the centreline velocity and the maximum slope $(du/dz)_{max}$. The centreline velocity typically changes from zero at the body, becoming negative in the reverse-flow region, and finally increases further downstream. The largest value of the maximum slope occurs for the profile right at the wake generating body. After a rapid reduction initially it decreases monotonically in the downstream direction.

The results of the present viscous investigation as well as the inviscid ones of Koch and Monkewitz & Nguyen reveal that the location of the downstream boundary of the absolutely unstable region is mainly dominated by the centreline velocity. That the stability characteristic of a profile is sensitive to the centreline velocity can also be seen from figure 16; the relative maximum of the ω_i curve occurs at the position with the highest reverse flow. The stability characteristic of the profiles located directly at the trailing edge however seems to be dominated by the maximum slope. In our investigation the rapid increase of $(du/dz)_{max}$ is accompanied by an increase in the temporal amplification rate. Monkewitz & Nguyen (1987) systematically varied the centreline velocity and the slope of their velocity profiles. In terms of their classification we have a set of profiles with a large initial shear-layer thickness. They found that for profiles with zero centreline velocity and a very thin initial shear-layer thickness the temporal amplification is negative, indicating convective instability.

From the results of the numerical simulation we know that the initially selected

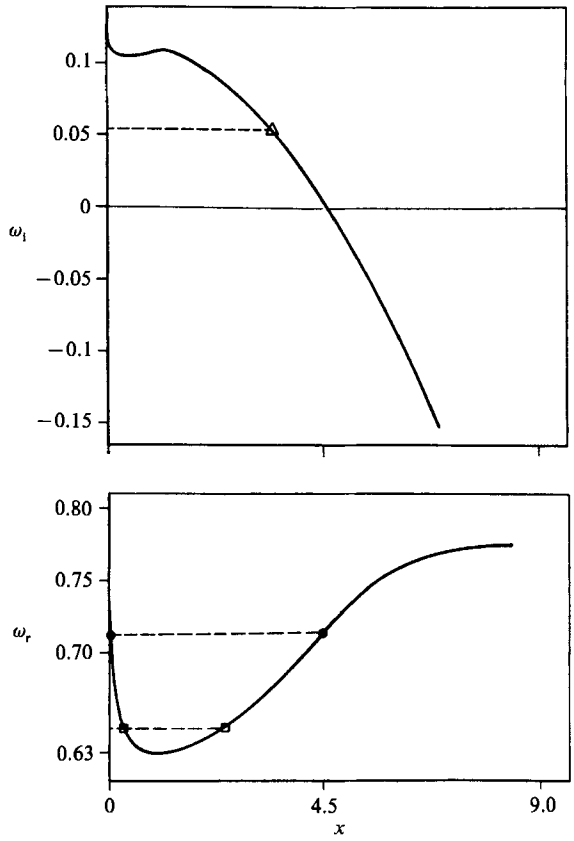

FIGURE 16. Frequency ω_r and temporal amplification rate ω_i at the branch-point singularities: □, onset frequency; △, corresponding amplification rate; and ●, saturation frequency of the numerical simulation.

frequency changes during the wake development. Therefore, regarding the frequency selection criteria we must differentiate between the selection of the onset frequency and the frequency in the saturation state; linear stability analysis is most appropriately applied to the onset of instability. The squares and the triangle in figure 16 mark the onset frequency and the corresponding temporal amplification rate obtained from the numerical simulation in the linear growth region (see figure 4). Neither values appears on the stability curves at the same x-position. This shows that none of the velocity profiles in the near wake can predict correctly both the frequency and the temporal amplification rate for the onset of instability. It appears therefore, for the invetigated flow field, that no selection criterion based on local wake properties can be derived.

From figure 16 it can be seen that all frequencies predicted by the stability theory in the region of absolute instability are in reasonable agreement with the frequencies found in the numerical simulation. Therefore it will be interesting to see to which prediction the selection criteria, described in § 1, will lead, especially for the variation of the base-bleed coefficient.

Koch's criterion was developed to predict the frequency only in the saturation state. He suggests that the flow in the saturation state is dominated by a local resonance occurring at the transition from local absolute instability to local convective instability ($\omega_i = 0$). Since this criterion is based on the linear stability

	Onset of instability		Saturation state		Error in %	
$Re = 200$	St_{on}	ω_i	St_{sat}	ω_i	St	ω_i
Numerical simulation	0.1032	0.053	0.11339	0	—	—
Initial-resonance criterion	0.118	0.138	—	—	14	160
Max.-growth-rate criterion	0.1006	0.110	—	—	2.5	107
Koch's criterion	—	—	0.1146	0	1.06	0

TABLE 1. Summary of the predictions of the selection criteria

analysis it should therefore be applied only in the vicinity of the critical Reynolds number, because here the saturation amplitudes are small. However W. Koch (1987, private communication) further suggests that this criterion can also be applied for supercritical Reynolds numbers, because he assumes that the flow in a nonlinear saturation state is still dominated by a local resonance, which has a frequency very close to the one predicted by linear theory applied to the basic steady state. Given a flow of type 'AB', where the absolutely unstable region extends up to the wake generating body, the initial-resonance criterion, introduced by Monkewitz & Nguyen (1987) and the maximum-growth criterion, proposed by Pierrehumbert (1984) always predict a frequency and a corresponding positive temporal amplification rate selected in the linear state. With both these criteria the saturation frequency can only be predicted if the frequency does not change during the wake development. It is clear from the numerical simulation that this does not hold true for the investigated flow. Consequently the initial-resonance criterion and the maximum-growth criterion can only be used for the prediction of the onset frequency and its amplification rate. The shape of the ω_i curve in figure 16 shows that the initial-resonance criterion and the maximum-growth criterion coincide. However in addition the ω_i curve has a relative maximum and for completeness we related the maximum-growth criterion also to this distinguished point.

The predictions of the selection criteria are summarized in table 1. In addition to the selected Strouhal number St and the corresponding amplification rate ω_i, the deviation of these predictions from the values obtained by the numerical simulation are presented. It can be seen from table 1 that the initial-resonance criterion and the maximum-growth criterion predict an onset frequency that differs by 14% and 2.5% respectively from the value of the numerical simulation. However the corresponding temporal amplification rate deviates by more than 100% for both selection criteria. We also recognize that Koch's criterion predicts a saturation-state frequency that differs by 1.06%. A further discussion of the validity of any selection criterion based on local wake properties will be presented in §7 after base bleed has been applied as a control parameter in the next section.

Figure 17 shows a comparison between the perturbation streamlines obtained from the numerical simulation in the linear growth region (figure 17*a*, which has already been discussed in §4) and the perturbation streamlines computed from a symmetric-mode eigenvector (figure 17*b*) of the u-velocity profile at $x = 4.0$. Both plots reveal that the vortex centres are located on the wake centreline. Therefore the structure of the perturbation flow, corresponding to the onset of the instability, can be predicted qualitatively by the local linear stability analysis. This structure was also found by Jackson (1987) in wakes at the critical Reynolds number using a global, linear stability analysis.

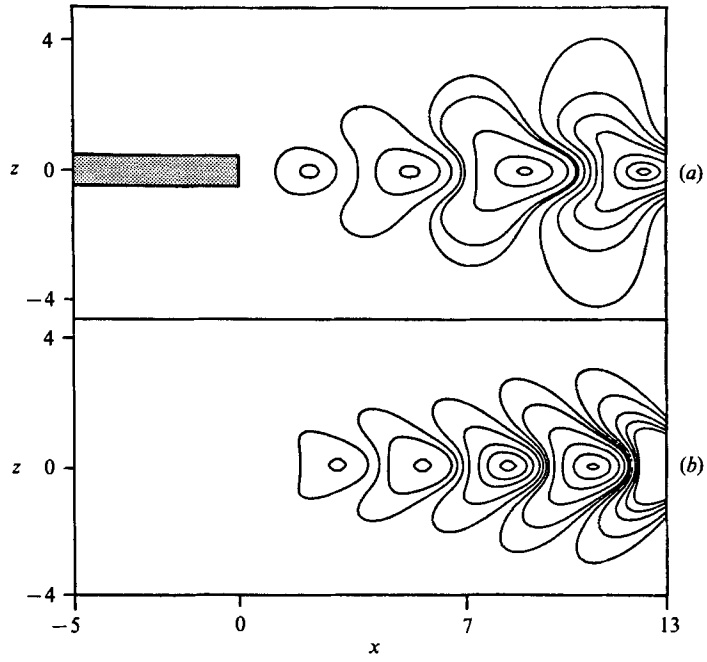

FIGURE 17. Instantaneous perturbation streamlines from (*a*) the numerical simulation in the linear growth region and (*b*) the stability analysis.

6. Wake control

Base bleed can be applied in the numerical simulation of the wake as a control parameter. It is well known from experimental investigations, e.g. Wood (1964, 1967), Bearman (1967) and Michel & Kost (1982) that sufficient base bleed leads to a reduction of base drag. This effect is accompanied by the decay of the strength of the vortex street and the change of the pure-frequency vortex street to a band of amplified frequencies in the wake. A direct comparison between these experiments and our numerical investigations will however not be possible because the experiments were carried out at very high Reynolds numbers with turbulent flows, whereas we investigate unsteady laminar flows at the Reynolds number $Re = 200$.

In the numerical simulation we apply several bleed coefficients

$$c_q = \frac{m^*}{u_\infty^* D^*}, \tag{22}$$

where m^* is the mass flow rate divided by density and for unit depth which is blown into the wake at the base of the plate. All simulations with base bleed are started from the quasi-steady solution of the 'natural' wake development (see figure 4). The base bleed is produced numerically in such a way that at all grid points located at the base, except the upper and lower one, the no-slip condition is replaced by a constant u-velocity component depending on the bleed coefficient.

Similar to the wake development described in §4 the simulations for several bleed coefficients show the development to a quasi-steady state, followed by a linear growth and transition region which finally leads to a saturation state. For two bleed coefficients, streamline plots and u-velocity profiles of the quasi-steady and saturation state are shown in figures 18 and 19. It can be seen that for the higher

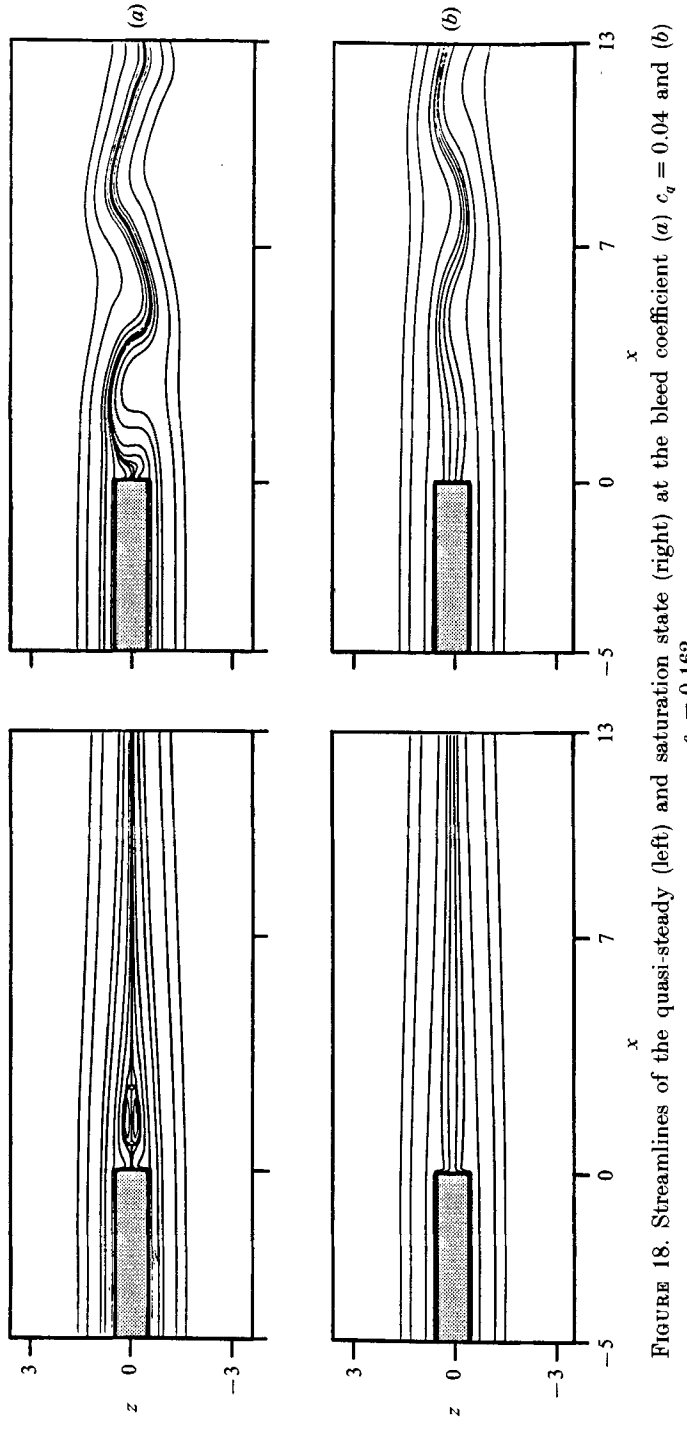

FIGURE 18. Streamlines of the quasi-steady (left) and saturation state (right) at the bleed coefficient (*a*) $c_q = 0.04$ and (*b*) $c_q = 0.162$.

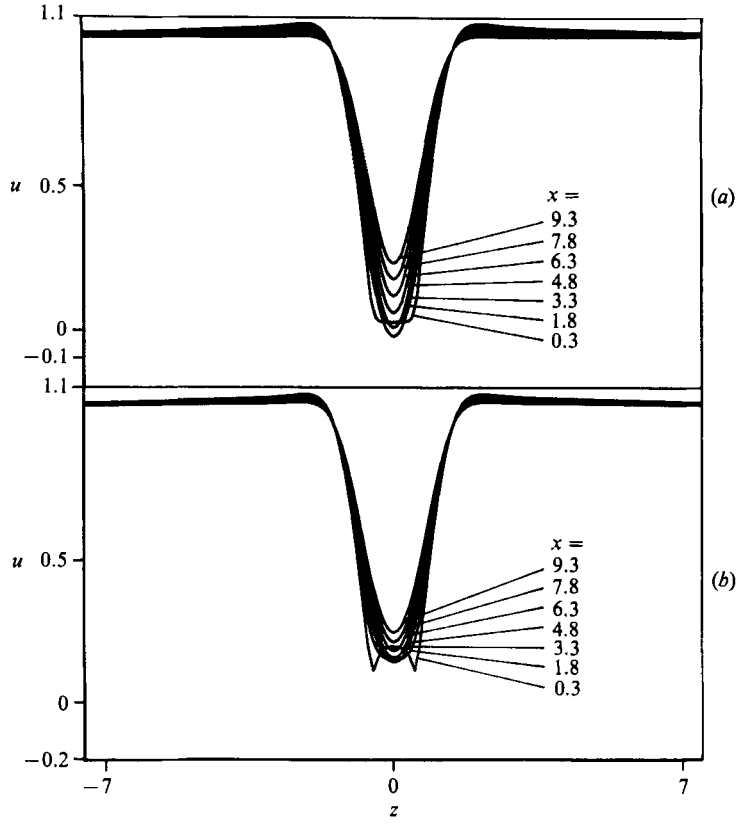

FIGURE 19. u-Velocity profiles of the quasi-steady state at (a) $c_q = 0.04$ and (b) $c_q = 0.162$.

bleed coefficient the amplitudes of the fluctuations in the saturation state are reduced in the near-wake region. The exponential temporal amplification rate ω_i of the selected onset frequency is reduced linearly with increasing bleed coefficient, as shown in figure 20. If the straight line in figure 2 is extrapolated (dashed line), a critical bleed coefficient of $c_q = 0.214$ can be determined, where the temporal amplification is zero. This means that for higher bleed coefficients than $c_{q_{\text{crit}}}$, fluctuations are temporally damped. To verify this we applied a bleed coefficient of $c_q = 0.24 > c_{q_{\text{crit}}}$. This simulation reaches a state where the maximum time derivative in the flow field stays at a constant level of 10^{-9} and no temporal amplification of fluctuations can be detected. Before this flow field is investigated in more detail some comments on the global flow behaviour, described by the numerical simulation, should be made. According to the definition of absolute instability the conclusion could be drawn that the wake flow at a control parameter, where disturbances are temporally amplified at a fixed position, is absolutely unstable. However, the concept of absolute and convective instability is purely local and therefore the global stability characteristic should not be referred to as absolutely unstable. It is more appropriate to describe the global flow under these circumstances as a self-excited oscillator. If no perturbations are temporally amplified the global flow will behave either as a spatial amplifier or will be completely stable. In the terminology used here the control parameter, at the transition from the behaviour as an amplifier to an oscillator, is called the critical control parameter.

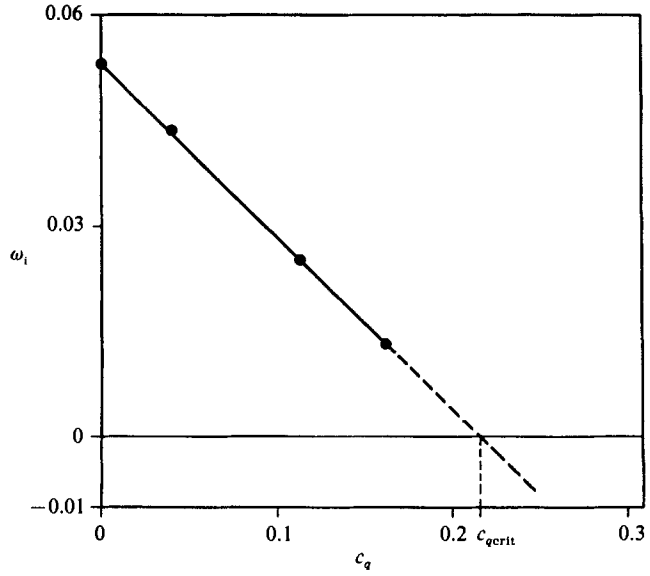

FIGURE 20. Exponential temporal amplification rate ω_i as a function of the bleed coefficient c_q.

To determine whether the flow at $c_q = 0.24$ is an amplifier or completely stable we investigate the spatial development of fluctuations. In the simulation, where the system of equations (16) is solved to an accuracy of $\epsilon = 10^{-9}$, initially no spatial amplification of fluctuations can be detected. However if the flow behaves as an amplifier it will depend strongly on the magnitude of the background disturbance level. If this is too low it is possible that the spatial amplification of fluctuations cannot be detected. For this reason the 'numerical fluctuation level' is increased step by step by increasing ϵ. The introduction of higher fluctuations provides a better means of detecting the presence of spatial amplification. For this investigation the u-velocity over time at several streamwise positions in the wake located at a fixed $z = 0.625$ are recorded. An analysis of these signals revealed that the r.m.s.-value was increased in the downstream direction, indicating spatial amplification.

The change of the onset and saturation frequency with the bleed coefficient is shown in figure 21. From the numerical investigation described in §4 we know that the change of the onset frequency leading to the saturation frequency is due to nonlinear effects. According to figure 21, showing that the difference between onset and saturation frequency is reduced with increasing bleed coefficient, it follows that the influence of nonlinearity should also be reduced. If we extrapolate both straight lines in figure 21 to higher bleed coefficients we get a point of intersection at the critical bleed coefficient $c_{q_{crit}}$, predicted from figure 20; at this point the onset and saturation frequency are identical.

A comparison with the experimental investigation of Strykowski (1986) reveals that an increasing bleed coefficient has a similar influence on the wake flow as a decreasing Reynolds number. Strykowski (1986) suggests that at subcritical Reynolds numbers the wake behind a circular cylinder can behave as a spatial amplifier ($\omega_i < 0$), whereas at supercritical Reynolds numbers it is similar to a self-excited oscillator ($\omega_i > 0$). He also found that at the critical Reynolds number the onset and saturation frequency are identical and for increasing Reynolds number the difference between these frequencies increases linearly.

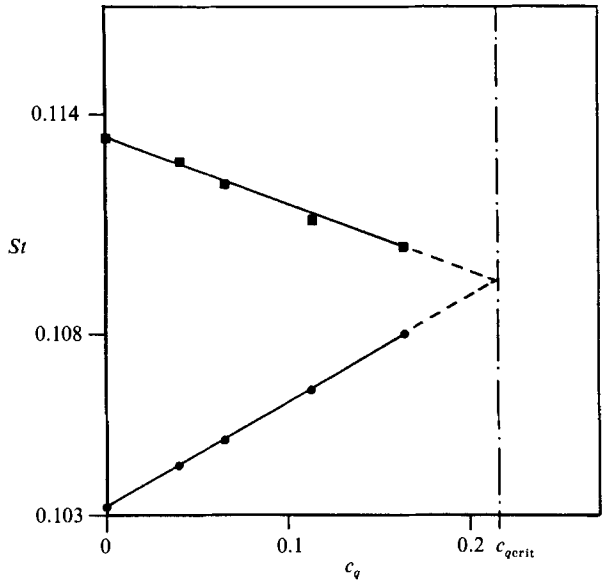

FIGURE 21. Onset (●) and saturation frequency (■) as a function of the bleed coefficient c_q.

We shall now investigate the quasi-steady states of the simulations with different bleed coefficients using local, linear stability analysis to see whether it can predict the transition of the global stability characteristic. For this purpose we again track the location of the branch-point singularities of the dispersion relation for complex frequency and wavenumber.

The frequency ω_r and the temporal amplification rate ω_i at these singularities are plotted in figure 22. Here, for comparison, the eigenvalues of the natural wake development already shown in figure 16 are plotted again. It can be seen from figure 22 that the ω_i curve for one bleed coefficient in the absolutely unstable area always lies under the ω_i curve corresponding to the next lower bleed coefficient. This shows in principle that increasing the bleed coefficient reduces the temporal amplification rate. However, we note that the ω_i curve corresponding to the bleed coefficient $c_q = 0.24$, for which the numerical simulation indicated no temporally amplifying perturbations, maintains a small region of absolute instability near the body. This indicates, as already discussed by Chomaz, Huerre & Redekopp (1987) and Monkewitz (1988), that according to local stability analysis the absolutely unstable region must have a finite size before the flow can behave as an oscillator. The same result could be obtained by variation of the Reynolds number (see Hannemann 1988). This indicates that local stability analysis can only give a lower bound on the critical control parameter (i.e. Reynolds number) at which the temporal amplification rate of the global non-parallel wake flow becomes positive. The shape of the ω_i curves also indicates that for a bleed coefficient between $c_q = 0.065$ and $c_q = 0.113$ a flow may exist that is initially absolutely unstable, followed subsequently downstream by regions of convective, absolute and finally convective instability.

The shape of the ω_i curves shows that the temporal amplification rate is always a maximum directly at the trailing edge of the plate. In the downstream direction it first decreases and then reaches a local maximum before it decreases again monotonically. From figure 22 it can also be seen that the velocity profiles located directly behind the trailing edge are not as highly influenced by the base bleed as the

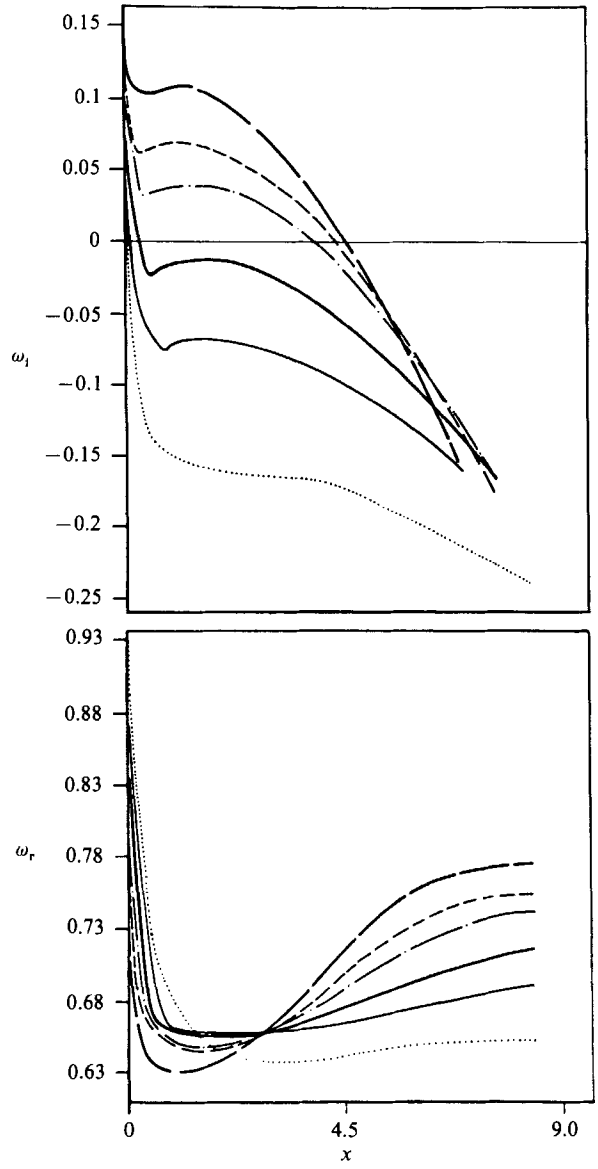

FIGURE 22. Frequency ω_r and temporal amplification rate ω_i at the branch point singularities: ——, natural wake development; – – –, $c_q = 0.04$; –·–·–, $c_q = 0.065$; ——, $c_q = 0.11375$; ——, $c_q = 0.1625$; · · · · · ·, $c_q = 0.243$.

profiles located further downstream, where the temporal amplification rate is more strongly decreased with increasing bleed coefficient. The reason for this can be found in the particular shape of the velocity profile at the trailing edge of the plate. As already described at the beginning of this section the base bleed is performed numerically in such a way that all points at the base have a constant u-velocity component except the upper and lower points; here the no-slip condition is maintained. Therefore the u-velocity profile at the trailing edge always has two points where the velocity is zero. The stability investigations have shown that the minimum velocity value of the profile is one indication of whether the profile is

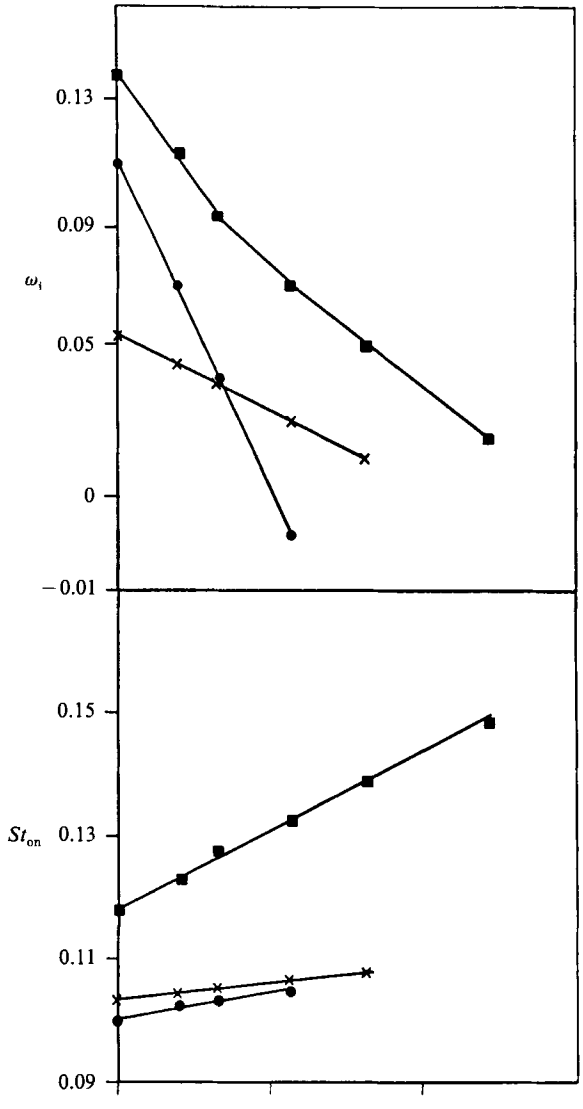

FIGURE 23. Comparison of the onset frequency St_{on} and temporal amplification rate, for the onset of the instability, by the initial-resonance criterion (■) and the maximum-growth criterion (●) with the values obtained by the numerical simulation (×).

absolutely or convectively unstable. Independent of the bleed coefficient the minimum velocity value at the trailing edge is zero and therefore this profile always has a relatively higher temporal amplification rate than the profiles further downstream where, for increasing bleed coefficient, the wake defect is more and more reduced. The shape of the ω_i and ω_r curves can also be used to determine how parallel the flow field is, because changes in the eigenvalue as a function of the downstream direction is an indication of how much the velocity profiles change. Based on this criterion we find that for $x \geqslant 2$ the wake becomes more parallel, especially for increasing bleed coefficient; however for $0 < x \leqslant 2$ the wake is still highly non-parallel.

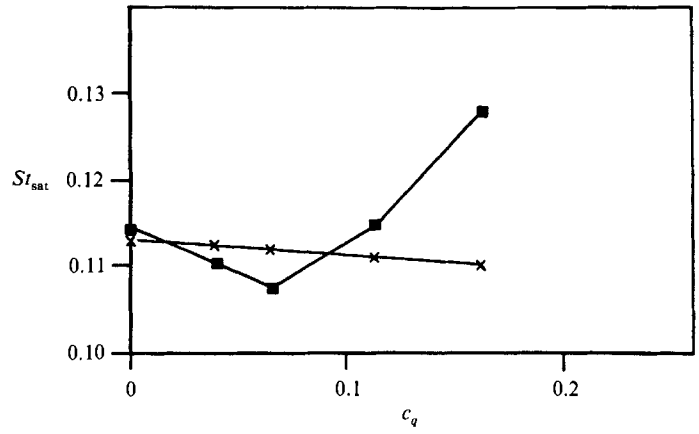

FIGURE 24. Predicted saturation frequency St_{sat} with Koch's criterion (■) in comparison with the frequency obtained by the numerical simulation (×).

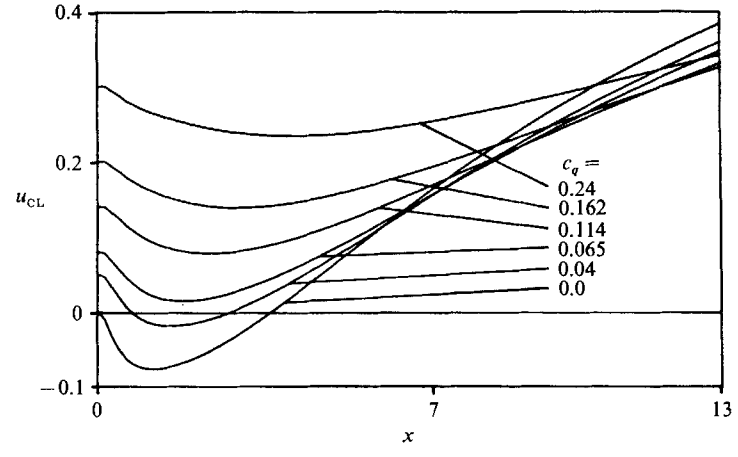

FIGURE 25. Centreline velocity u_{CL} as a function of the base-bleed coefficient c_q and the coordinate x.

The development of the onset frequencies and corresponding amplification rate as a function of the bleed coefficient can qualitatively be well described by the initial-resonance criterion and the maximum-growth criterion; the latter predicts frequencies that are also quantitatively close to the values of the numerical simulation (see figure 23). The predicted temporal amplification rates, on the contrary, differ completely from the ones obtained by the numerical simulation. It turns out that the agreement for $c_q = 0.065$ can be regarded as coincidental.

The prediction of the saturation frequency using Koch's criterion leads, for the natural wake development and the two lowest bleed coefficients, to values that are very close to the frequencies of the numerical simulation; however for the higher bleed coefficient, when the transition point from absolute to convective instability moves into the region close to the body, the predictions become increasingly worse (see figure 24). A possible explanation for this is that, owing to the special shape of the u-velocity profiles at the trailing edge induced by the modelling of the base bleed, the stability analysis no longer describes the wake instability but rather the shear-layer instability occurring at the transition from the base-bleed jet to the separating

boundary layer. Such shear instabilities commonly have higher frequencies than the wake instabilities. Monkewitz & Nguyen (1987) give an upper limit of $u_{CL} = 0.09$ below which velocity profiles can be absolutely unstable. The centreline velocity u_{CL} is shown in figure 25 as a function of the bleed coefficient c_q and the coordinate x. Comparing figure 22 with figure 25, we confirm the value found by Monkewitz & Nguyen (1987). For the velocity profiles next to the plate at high bleed coefficient (where the minimum velocity does not occur on the centreline) (see figure 19) this criterion is also satisfied.

7. Summary and conclusions

The numerical simulation of the development of the Kármán vortex street behind a flat plate at supercritical Reynolds number $Re = 200$ reveals that this development can be subdivided into four regions (see figure 4). Starting from the quasi-steady solution we can observe the exponential temporal growth of a perturbation at one pure frequency in the linear region. It should be reiterated that no artificial perturbation must be introduced to initiate the amplification process, apart from the 'numerical fluctuation level' caused by the spatial discretization, the choice of the initial condition and the accuracy with which the system of equations (16) is solved.

By investigating the velocity signals over time, recorded at many points in the wake, it was found that the selected frequency and the corresponding temporal amplification rate is the same everywhere in the flow field (figure 7). An exception, discussed in §4, occurs in the u-velocity components recorded on the centreline. However, the first harmonic of the onset frequency and the double growth rate occurring at the centreline for $t \approx 100$ are consequences of the nonlinearity causing the structure change of the perturbation flow and cannot be regarded as the appearance of an independent second frequency in the wake development. Given this result, the linear growth region could be subdivided into a region $t < 100$ where the flow behaves purely linearly and a second region $100 < t < 240$ where the effect of the nonlinearity can already be detected but is so small that it does not influence either the growth rate or the onset frequency.

The fact that a single frequency with a well-defined temporal amplification rate is dominant during linear growth indicates that the development to the vortex street is governed by a true time-growing instability, i.e. the global flow behaves like a self-excited oscillator.

Using base bleed as a control parameter in the numerical simulation it is possible to reduce the temporal amplification rate until it is forced to be negative (see figure 20), thereby showing the transition from an oscillator to an amplifier. Experimental investigations using other devices, e.g. the splitter plate used by Roshko (1954) or the 'control cylinder' used by Strykowski & Sreenivasan (1985) and Strykowski (1986), also show that the formation of the vortex street behind circular cylinders could be suppressed. For a review of other two-dimensional devices that influence the wake see Tanner (1975). We suggest that these devices change the stability characteristic of the flow in a similar manner to the base bleed.

The numerical simulation provides the quasi-steady solution which we believe is the appropriate basic state for an investigation using linear stability analysis. In particular we use linear, local stability analysis following the recent investigations by Koch (1985), Triantafyllou *et al.* (1986), Monkewitz & Nguyen (1987) and Monkewitz (1988). However, in all of these previous investigations the near wake was modelled

with analytic functions whereas the present study uses profiles obtained directly from the Navier–Stokes equations. The question immediately arises of the extent to which local theory can be applied to a non-parallel flow and produce meaningful physical results; this investigation was undertaken to answer that question. From the comparison between the results of the numerical simulation and the predictions of the stability analysis, it follows that in spite of the simplifying assumptions the stability analysis can be used for a qualitative description of the investigated wake properties. It predicts qualitatively the structure of the perturbation flow for the onset of the instability (see figure 17). The stability curves presented in figure 16 and figure 22 reveal that the Orr–Sommerfeld analysis predicts the correct trend of decreasing temporal amplification rate with increasing bleed coefficient.

The ω_i curves indicate that only a part of the wake flow near the body is absolutely unstable. The stability analysis predicts a band of frequencies that can grow locally, corresponding to the positive part of the ω_i curve. To predict which of these local modes is selected for the vortex-shedding frequency different selection criteria have been proposed by several authors. A classification of these selection criteria was needed because, as the numerical simulation shows, the onset frequency selected at the beginning of the linear growth region changes by approximately 10% during the wake development until the saturation frequency is reached. Strykowski (1986) found, for the wakes behind circular cylinders, that this change increases with increasing Reynolds number and is approximately 42% at $Re = 80$, indicating that the change is an effect that cannot be neglected. The classification, discussed in §5, was based on a flow field of type 'AB'. It is clear that for a flow of type 'AF', which according to Monkewitz & Nguyen (1987) is also relevant for wake flows, the initial-resonance criterion of Monkewitz & Nguyen acts similarly to Koch's criterion. The difference is that the frequency would be predicted by the first transition point from convective to absolute instability and not by the last one, as according to Koch. Under the assumption used by Koch that the linear resonance frequency does not differ very much from the nonlinear one, the initial-resonance criterion could also be used for the prediction of the saturation frequency. It should be mentioned that, owing to the frequency changes occurring during the wake development, the linear resonance frequency must not be identical to the onset frequency. While Koch (1985) did not consider a flow of type 'AF', Monkewitz & Nguyen (1987) suggested for this type of flow that the initial-resonance criterion is more relevant in predicting the saturation frequency. Our application of the selection criteria to the investigated flow fields shows that the initial-resonance criterion and the maximum-growth criterion for the onset frequencies as well as Koch's criterion for the saturation frequencies (apart from the two highest bleed coefficients) can give a satisfactory prediction of how these quantities vary as a function of the bleed coefficient. The prediction of the temporal amplification rate using the initial-resonance criterion and the maximum-growth criterion appears to be too high in all cases investigated. It can be seen from the stability calculations that the maximum temporal growth rate is always much higher than the growth rate obtained from the global wake behaviour (i.e. numerical wake simulation). For this reason the critical control parameter (e.g. base-bleed coefficient or Reynolds numbers) cannot be obtained. For a better quantitative determination of the critical parameter the linear, global stability analysis as used by Jackson (1987) should be applied.

The authors wish to express sincere thanks to Dr W. Koch and Dr P. J. Strykowski for many simulating discussions concerning this work and their critical review of the manuscript.

REFERENCES

BEARMAN, P. W. 1967 The effect of base bleed on the flow behind a two-dimensional model with a blunt trailing edge. *Aero. Quart.* **18**, 207–224.

BECHERT, D. W. 1985 Excitation of instability waves. *Z. Flugwiss. Weltraumforsch.* **9**, 356–361.

BERS, A. 1975 Linear waves and instabilities. In *Physique des Plasmas* (ed. C. DeWitt & J. Peyraud), pp. 117–213. Gordon and Breach.

BETCHOV, R. & CRIMINALE, W. O. 1966 Spatial instability of the inviscid jet and wake. *Phys. Fluids* **9**, 359–362.

BRAZA, M., CHASSAING, P. & HA MINH, H. 1986 Numerical study and physical analysis of the pressure and velocity fields in the near wake of a circular cylinder. *J. Fluid Mech.* **165**, 79–130.

BRIGGS, R. J. 1964 Electron-stream interaction with plasmas. *Research Monograph* 29. MIT Press.

CHOMAZ, J. M., HUERRE, P., REDEKOPP, L. G. 1987 Models of hydrodynamic resonances in separated shear flows. In *Proc. 6th Symp. on Turbulent Shear flows, Toulouse, France, Sept. 7–9.*

DAVIS, R. W. & MOORE, E. F. 1982 A numerical study of vortex shedding from rectangles. *J. Fluid Mech.* **116**, 475–506.

DRAZIN, P. G. & REID, W. H. 1981 *Hydrodynamic Stability.* Cambridge University Press.

GASTER, M. 1968 Growth of disturbances in both space and time. *Phys. Fluids* **11**, 723–727.

GENTZSCH, W. & SCHWAMBORN, D. 1985 Das Problem der numerischen Diffusion bei der Lösung von Modellgleichungen der Strömungsmechanik. *DFVLR IB* 221-85 A15.

GOTTLIEB, D., HUSSAINI, M. Y. & ORSZAG, S. A. 1984 Theory and applications of spectral methods. In *Spectral Methods for Partial Differential Equations* (ed. R. G. Voigt *et al.*), Philadelphia.

HANNEMANN, K. 1988 Numerische Simulation und Stabilitätstheoretische Untersuchung des absolut und konvektiv instabilen Nachlaufs. *DFVLR FB* 88-09.

HANNEMANN, K., LYNN, T. B. & STRYKOWSKI, P. J. 1986 Experimental investigation of the wake behind a flat plate with and without the influence of base bleed. *DFVLR IB* 221-86 A26.

HANNEMANN, K. & OERTEL, H. 1986 Das Nachlaufstabilitätsproblem. *DFVLR IB* 221-86 A05.

HANNEMANN, K. & OERTEL, H. 1987 Linear stability analysis and nonlinear numerical simulation of wake flows. In *Proc. Intl Conf. on Fluid Mechanics, Beijing, China, July 1–4*, pp. 667–672.

HUERRE, P. 1985 Spatio-temporal instabilities in closed and open flows. In *Proc. Intl Workshop on Instabilities and non-Equilibrium structures, Valparaiso, Chile, December 16–21.*

HUERRE, P. & MONKEWITZ, P. A. 1985 Absolute and convective instabilities in free shear layers. *J. Fluid Mech.* **159**, 151–168.

JACKSON, C. P. 1987 A finite-element study of the onset of vortex shedding in flow past variously shaped bodies. *J. Fluid Mech.* **182**, 23–45.

KHOSLA, P. K. & RUBIN, S. G. 1981 A conjugate gradient iterative method. *Computers and Fluids* **9**, 109–121.

KOCH, W. 1983 Organized structures in wakes and jets – an aerodynamic resonance phenomenon? In *Turbulent Shear Flows 4* (ed. L. J. S. Bradbury, F. Durst, B. E. Launder, F. W. Schmidt & J. H. Whitelaw). Springer.

KOCH, W. 1985 Local instability characteristics and frequency determination of self-excited wake flows. *J. Sound Vib.* **99**, 53–83.

KOCH, W. 1986 Direct resonances in Orr–Sommerfeld problems. *Acta Mech.* **58**, 11–29.

KOVASZNAY, L. S. G. 1949 Hot-wire investigation of the wake behind cylinders at low Reynolds numbers. *Proc. R. Soc. Lond.* A **198**, 174–190.

LANDAU, L. D. & LIFTSHITZ, E. M. 1959 *Fluid Mechanics*, vol. 6. Pergamon.

LAURIEN, E. 1986 Numerische Simulation zur aktiven Beeinflussung des laminar-turbulenten Übergangs in der Plattengrenzschichtströmung. *DFVLR-FB* 86-05.

MATTINGLY, G. E. & CRIMINALE, W. O. 1972 The stability of an incompressible two-dimensional wake. *J. Fluid Mech.* **51**, 233–272.

MICHEL, G. W. & KOST, F. H. 1982 The effect of coolant flow on the efficiency of a transonic HP turbine profile suitable for a small engine. *American Society of Mechanical Engineers* 82-GT-86.

MONKEWITZ, P. A. 1988 The absolute and convective nature of instability in two-dimensional wakes at low Reynolds numbers. *Phys. Fluids* **31**, 999–1006.

MONKEWITZ, P. A. & NGUYEN, L. N. 1987 Absolute instability in the near-wake of two-dimensional bluff bodies. *J. Fluids and Structures* **1**, 165–184.

MONKEWITZ, P. A. & SOHN, K. D. 1986 Absolute instability in hot jets and their control. *AIAA Paper* 86-1882.

NASH, J. F., QUINCEY, V. G. & CALLINAN, J. 1963 Experiments on two-dimensional base flow at subsonic and transonic speeds. *Aero. Res. Counc. R. & M.* 3427.

NGUYEN, L. N. 1986 Frequency selection in jets and wakes. M.S. thesis, University of California, Los Angeles.

PIERREHUMBERT, R. T. 1984 Local and global baroclinic instability of zonally varying flow. *J. Atmos. Sci.* **41**, 2141–2162.

PROVANSAL, M., MATHIS, C. & BOYER, L. 1987 Bénard–von Kármán instability: transient and forced regimes. *J. Fluid Mech.* **182**, 1–22.

ROSHKO, A. 1954 On the drag and shedding frequency of two-dimensional bluff bodies. *NACA TN* 3169.

SATO, H. & KURIKI, K. 1961 The mechanism of transition in the wake of a thin flat plate placed parallel to a uniform flow. *J. Fluid Mech.* **11**, 321–352.

SCHLICHTING, H. 1982 *Grenzschicht-Theorie* 8th edn. Auflage, Karlsruhe: Braun.

SCHWARZ, H. R., RUTISCHAUSER, H. & STIEFEL, E. 1968 *Matrizen-Numerik*. Stuttgart: B. G. Teubner.

STEPHENS, A. B., BELL, J. B., SOLOMON, J. M. & HACKERMAN, L. B. 1984 A finite difference Galerkin formulation for the incompressible Navier–Stokes equations. *J. Comp. Phys.* **53**, 152–172.

STRYKOWSKI, P. J. 1986 The control of absolutely and convectively unstable shear flows. Doctoral thesis, Yale University, New Haven, CT.

STRYKOWSKI, P. J. & SREENIVASAN, K. R. 1985 The control of transitional flows. *AIAA-paper* 85-0559 (presented at AIAA Shear Flows Control Conference, March 12–14, Boulder, Co).

STUART, J. T. 1960 On the non-linear mechanics of wave disturbances in stable and unstable parallel flows. *J. Fluid Mech.* **9**, 353–370.

STURROCK, P. A. 1958 Kinematics of growing waves. *Phys. Rev.* **112**, 1488–1503.

SUN, Y. C., SHEN, S. F. & ZHU, Z. 1988 A numerical simulation of the development behind a circular cylinder started from rest and a criterion for investigating unsteady separating flows. *Acta Mech.* (to appear).

TANNER, M. 1975 Reduction of base drag. *Prog. Aerospace Sci.* **16**, 369–384.

TRIANTAFYLLOU, G. S., TRIANTAFYLLOU, M. S. & CHRYSSOSTOMIDIS, C. 1986 On the formation of vortex streets behind stationary cylinders. *J. Fluid Mech.* **170**, 461–477.

TWISS, R. Q. 1951 On oscillations in electron streams. *Proc. Phys. Soc. Lond.* B **64**, 654–669.

TWISS, R. Q. 1952 Propagation in electron-ion streams. *Phys. Rev.* **88**, 1392–1407.

WOOD, C. J. 1964 The effect of base bleed on a periodic wake. *J. R. Aeronaut. Soc.* **68**, 477–482.

WOOD, C. J. 1967 Visualization of an incompressible wake with base bleed. *J. Fluid Mech.* **29**, 259–272.